Student Developed Meteorological Radar Network for the Western Part of Puerto Rico: First Node

by

Manuel A. Vega-Cartagena

A thesis submitted in partial fulfillment of the requirements for the degree of

MASTER OF SCIENCE
in
ELECTRICAL ENGINEERING

UNIVERSITY OF PUERTO RICO
MAYAGÜEZ CAMPUS
2007

Approved by:

_____	_____
H. Mario Ierkic, PhD Member, Graduate Committee	Date
_____	_____
Lionel R. Orama-Exclusa, PhD Member, Graduate Committee	Date
_____	_____
José G. Colom-Ustáriz, PhD President, Graduate Committee	Date
_____	_____
Walter Díaz, PhD Representative of Graduate Studies	Date
_____	_____
Isidoro Couvertier, PhD Chairperson of the Department	Date

ABSTRACT

This document summarizes the work done in developing the first node of a student designed X-band radar network in western Puerto Rico. The network proposed will improve coverage and resolution of the weather of western Puerto Rico through the implementation of low-cost and short-range radar systems. Modifications to commercially available Raytheon MK2 High Seas marine radars are presented as well as the sensitivity analysis performed. The modifications consisted of replacing the antenna, reducing the antenna pedestal's angular velocity, adding an internal calibration channel and replacing the data acquisition system. A case study where the initial data is compared with Nexrad and rain gauge data is presented. As a result, agreement between the three sensors was found. On the other hand, the resolution was improved more than 6 times when compared to NEXRAD. This will enhance the study of weather features in western Puerto Rico.

RESUMEN

Este documento resume el trabajo llevado a cabo en desarrollar el primer nodo de una red de sistemas de radares de banda X, diseñada por estudiantes, para la parte Oeste de Puerto Rico. La red propuesta mejorará la cobertura y resolución del Oeste de Puerto Rico a través de la implementación de sistemas de radares de bajo costo y alcance. Las modificaciones a un radar marino Raytheon MK2 “High Seas”, comercialmente disponible, serán presentadas. Dichas modificaciones consistieron en reemplazar la antena, reducir la velocidad angular del pedestal, añadir un canal de calibración interna y reemplazar el sistema de adquisición de datos. Un caso será presentado en el cual se comparan datos iniciales con datos del sistema Nexrad y datos de una red de pluviómetros. Se observó que los resultados de los tres sensores son similares. Por otro lado, la resolución fue mejorada por un factor de más de 6 veces. Se espera que esta mejora contribuya en el estudio del clima en la parte Oeste de Puerto Rico.

To the ALL . . .

ACKNOWLEDGEMENTS

During my graduate studies at the University of Puerto Rico at Mayagüez, several persons and institutions contributed directly and indirectly to my research. Without their support it would have been impossible for me to finish my work. That is why I wish to dedicate this section to recognizing their support.

First, I would like to start by expressing sincere gratefulness to Raisa Guzmán, my future partner in life, for standing beside me throughout the entire process. Without your support, love and understanding, this work would never have been possible.

I would like to thank Dr. José Colom and Dr. Lionel Orama for giving me the opportunity to perform this research. I would also like to thank Dr. Sandra Cruz-Pol and Dr. H. Mario Ierkic for their help as well. Also I would like to thank Dr. Eric Harmsen for supplying the Miradero rain gauge data.

From NASA Goddard Space Flight Center, Dr. Gerald Heymsfield, Dr. Lihua Li, Dr. Rafael Rincón and Shannon Rodríguez. Working with you greatly influenced this research, thank you.

Dr. Iván Baigés and Alfredo Moreu, your help made this work possible. Thank you for your interest in this work and for always being available.

The UPRM team, Víctor Marrero, Jorge Trabal (UMass), Pablo Lozada, Carlos Rodríguez, Ricardo Ríos, Juan Cordero, José Padovani, Soralis Pimentel and Manuel Cruz. You al helped greatly in making this possible.

The NSF Grant 0313747 and NASA IDEAS provided the funding and the resources for the development of this research. Last, but definitely not the least, I would like to thank my family for their support.

Table of Contents

Table List

Figure List

Figures **Page**

1 INTRODUCTION

The goal of the National Science Foundation Engineering Research Center (ERC) for Collaborative Adaptive Sensing of the Atmosphere (CASA) is to explore and develop new methods for improving observation, detection and prediction of atmospheric phenomena [1]. CASA is focused on developing Distributed Collaborative Adaptive Sensing (DCAS) as a systems technology to improve our ability to monitor the earth's lower troposphere. It is comprised of four core partners: University of Massachusetts, Colorado State University, University of Oklahoma and University of Puerto Rico, Mayagüez.

Improving today's weather monitoring and forecasting requires an increase in both the resolution and volume coverage of observations in the lowest kilometers of the troposphere [2]. The proposed DCAS system will be created with a network of X-band radars taking into account the conditions previously stated. To achieve this type of system, a series of technology and full-system test-beds were planned and distributed throughout the different core partners. An innovative approach of the center was to integrate students from the four different campuses in a unique research experience under what has been called the Student Led Test-bed (SLT).

The SLT's main goals are to establish a Quantitative Precipitation Estimation (QPE) sensing network starting in western Puerto Rico. This network will take into consideration the coverage gaps from NEXRAD (TJUA), which is located in the eastern section of the island. It is expected that with more coverage and better resolution, a significant improvement in precipitation estimates for western Puerto Rico will be achieved. This thesis

summarizes the work performed while developing the first node (PR1) of the DCAS radar network being developed for Puerto Rico. It covers all aspects taken into account during the design, implementation and initial testing of PR1.

1.1 Motivation

Current approaches to sampling the first three kilometers of the troposphere are physically limited in their ability to provide the required resolution and coverage. The current state of the art is comprised of radars used to cover large distances up to 240 km, as in the case of the WSR-88D (referred to as NEXRAD). Long range radars introduce limitations due to the earth's curvature. As the range increases away from the radar, the earth's surface curves away under the radar's beam creating an inability to observe the atmosphere close to the earth's surface. Atmospheric phenomena can go unobserved, literally lying "under the radar".

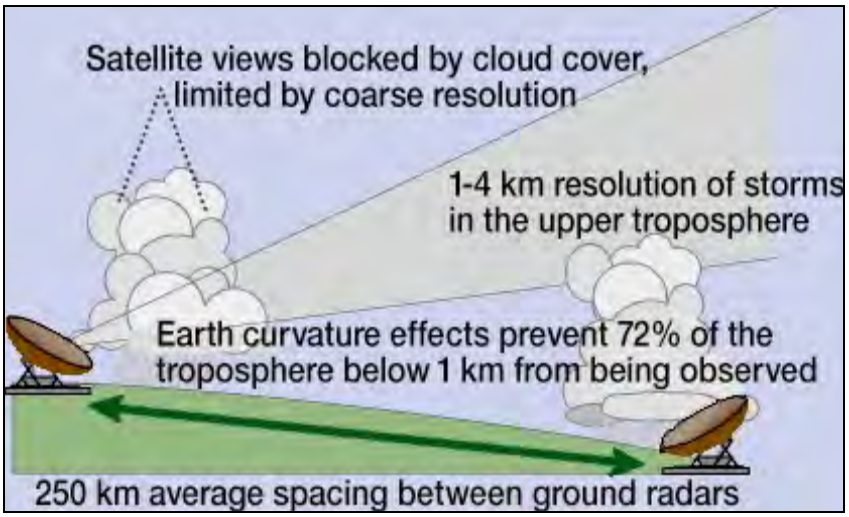

Figure 1-1 Radar beam overshooting rain clouds due to Earth's curvature effect [1].

Furthermore, obstacles such as mountain ranges may also block the radar's beam preventing observation of events beyond the obstacle. The network of shorter range (~25 km) X-band radars proposed by CASA could overcome the issues mentioned above. It is expected that with more coverage and better resolution, a significant improvement in precipitation estimates for western Puerto Rico will be achieved.

1.2 Objectives

The main objective of this research is to develop a short range, X-band, single polarization meteorological radar system at UPRM. This work required the modification of a marine radar for atmospheric purposes, testing, and preliminary data analysis. This system will be the first node of the network proposed by CASA's SLT and will be an integrated part of future QPE measurements for Puerto Rico's western coast. Being the first node, PR1 will lay the groundwork for future radar development at UPRM. Some components of PR1 such as the tower at the ECE building, transceiver, antenna could be modified/upgraded and reused in future projects, and therefore, bring down the cost of future radar research at UPRM.

On the other hand, the development of PR1 will provide new opportunities for undergraduate students to develop radar skills by engaging in a real life collaborative system design experience. Furthermore, PR1 may enable future graduate students to conduct QPE and/or attenuation studies using locally acquired data. In addition, PR1 can be the source of challenging projects to upgrade its capabilities.

1.3 Literature Review

Currently, ground based radars are installed on high mountains to get an obstruction-free beam angle view and reduce clutter contamination as much as possible [3]. Installing meteorological radars at these heights causes the loss of valuable information from the lower troposphere as the beam moves away from the site. For example, lets examine the case of the NEXRAD (WSR-88D) located in Cayey, Puerto Rico (TJUA). TJUA is located 851 meters over sea level, locating the beam well above 1 km in the western part (~110 km from TJUA) of the island [3], see Figure 1-2. This could cause errors in QPE since the measurements being made are not sampling hydrometeors located in the lower troposphere. An approach to solving this problem is currently being implemented by CASA [1]. CASA's approach is to install a DCAS network of X-band meteorological radars that will overcome the earth's curvature problem among other improvements.

In [4] [5], modified marine weather radar systems have been developed as low-cost solutions for precipitation measurement. One of the major drawbacks in keeping this type of systems low-cost is the use of logarithmic-detectors. Although this method is a cost-efficient one, it eliminates the capability of doing Doppler measurements, which are useful in clutter filtering and enable wind measurement capabilities. However, other methods such as clutter modeling and subtraction could be used as alternatives to reduce contamination from distributed targets [5]. Low-cost radar processors such as the one described in [4] are easily achievable since all calculations are based on digitizing the video signal, performing non-coherent pulse integration and retrieving the reflectivity factor (Z) based on the Rayleigh

radar equation [4]. Once we have Z, Z-R (reflectivity-rain rate) relationships are used to estimate precipitation.

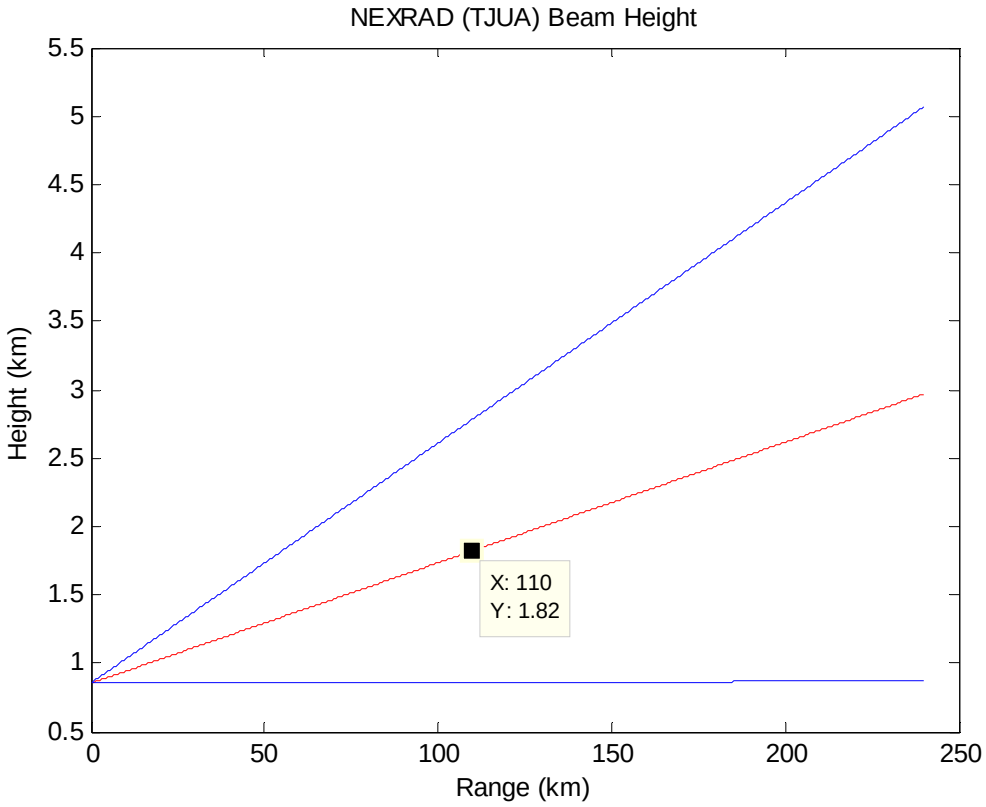

Figure 1-2 NEXRAD beam height using curved Earth surface model.

Moving to a higher operating frequency such as X-band introduces the advantages of developing lighter weight, lower cost and more flexible radar systems. However, operating at X-band requires the implementation of algorithms to compensate for the higher attenuation caused by hydrometeors [6]. An exact solution to this problem is the Hitschfeld and Bordan (HB) algorithm, although it has been demonstrated that it diverges rapidly for excessive attenuation when measurements are affected by errors such as offsets in radar calibration, uncertainties in drop size distribution (DSD), measurement noise and Z-R and k-R

relationships [7]. To overcome this defect, a modified HB algorithm has been developed using PIA as a constraint [7]. The SRT, developed for spaceborne radar applications provides the means for measurements of PIA [8]. This method presents a way to apply attenuation correction using a single polarization ground-based radar in mountainous terrain since it could be applied using returns from terrain as a reference, shown in Figure 1-3 [6] [9].

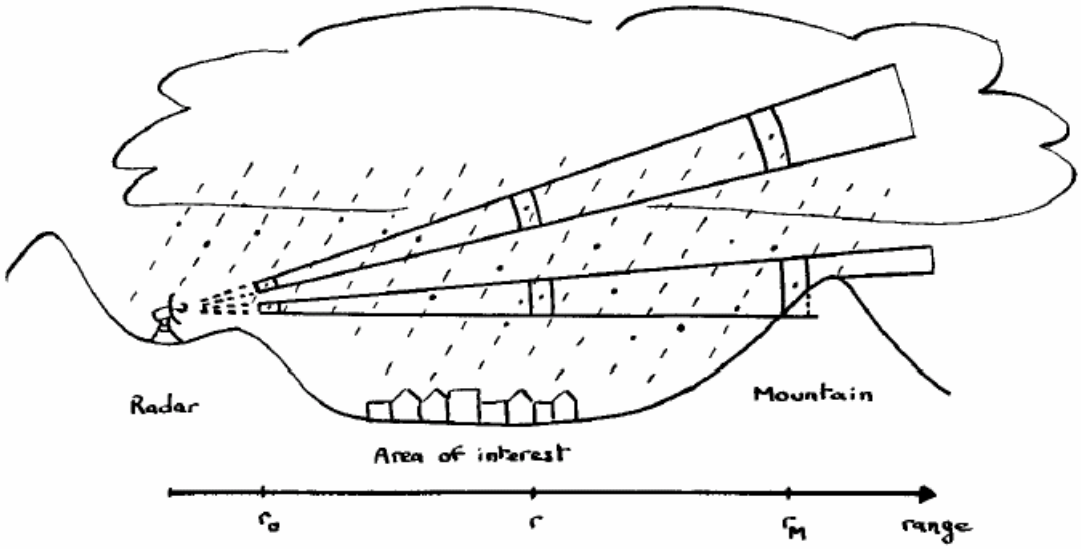

Figure 1-3 SRT using mountains as reference [6].

On the other hand, to improve measurement accuracy it is also important to eliminate calibration offsets. Although internal calibration does not allow absolute calibration, it provides constant monitoring of system parameters such as transmitted power and receiver gain [10]. Drifts and/or degradation of both of these parameters could bias the measurements. Therefore, the internal calibration channel plays an important role in making accurate measurements. Absolute calibration of the whole system can be performed using a known cross section such as a trihedral corner reflector [11].

1.4 Summary of Following Chapters

Chapter 2 develops the necessary background in basic radar theory. The point target radar equation all the way through to the weather radar equation is covered in this chapter along with basic microwave receiver design techniques. Chapter 3 deals with the design of PR1. It covers the initial sensitivity analysis and the modifications made to the "off-the-shelf" marine radar system. The fourth chapter presents a case study using PR1's initial data compared to, Nexrad, the Miradero rain gauge network and atmospheric soundings. It also describes the receiver calibration procedures. Conclusions and future work are presented in Chapter 5.

2 THEORETICAL BACKGROUND

2.1 Radar Parameters

2.1.1 Spatial Resolution

Essentially, radar systems make use of modulated waveforms and directive antennas to transmit electromagnetic energy into a specific volume in space to detect and/or study targets. A target may be any given object within the resolution volume. It is common within the radar community to classify radar systems according to their transmit waveforms. The two major types are continuous wave (CW) and pulsed radars. CW radars continuously emit electromagnetic energy and make use of separate transmit and receive antennas, while pulsed radars use a train of pulsed waveforms, Figure 2-1.

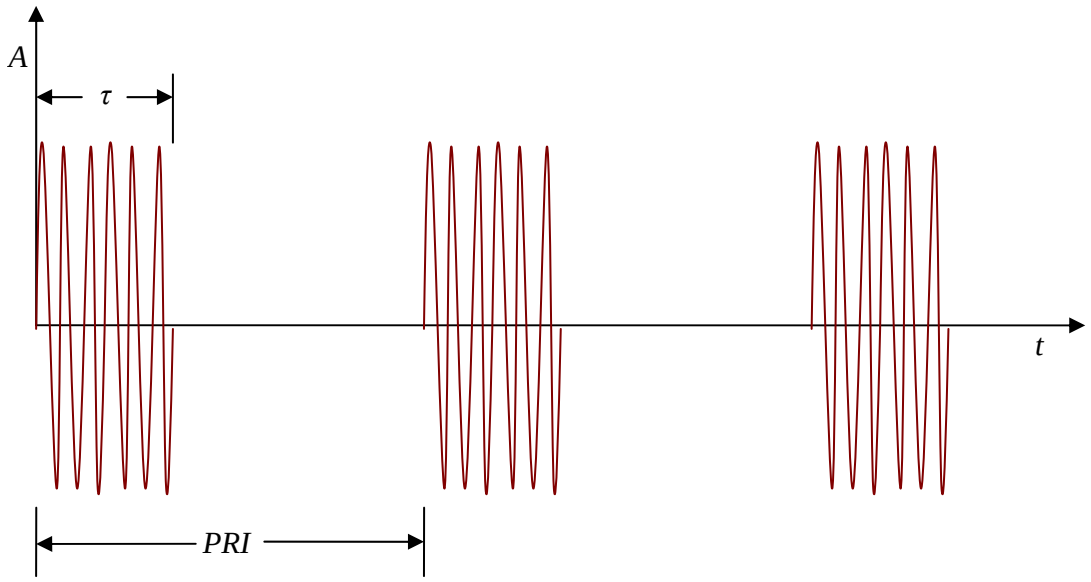

Figure 2-1 Pulsed radar waveform example.

When designing a pulsed weather radar system, one of the first requirements that set many other system parameters is the desired spatial resolution. Spatial resolution can be divided into two types, radial and azimuth. These two determine the radar's volume resolution, Figure 2-2. In a pulsed radar system, the radial resolution (ΔR) is determined by the width of the transmitted pulse, denoted by τ in Figure 2-1. Radial resolution is calculated using equation 2.1, where c is the speed of light and B is the pulse bandwidth. On the other hand, azimuth resolution is dictated by the antenna and calculated using equation 2.2, where θ is the antenna's half power beam width (HPBW) in radians and R is radial range.

$$\Delta R = \frac{c\tau}{2} = \frac{c}{2B} \qquad \textbf{2.1}$$

$$d = \theta R \qquad \textbf{2.2}$$

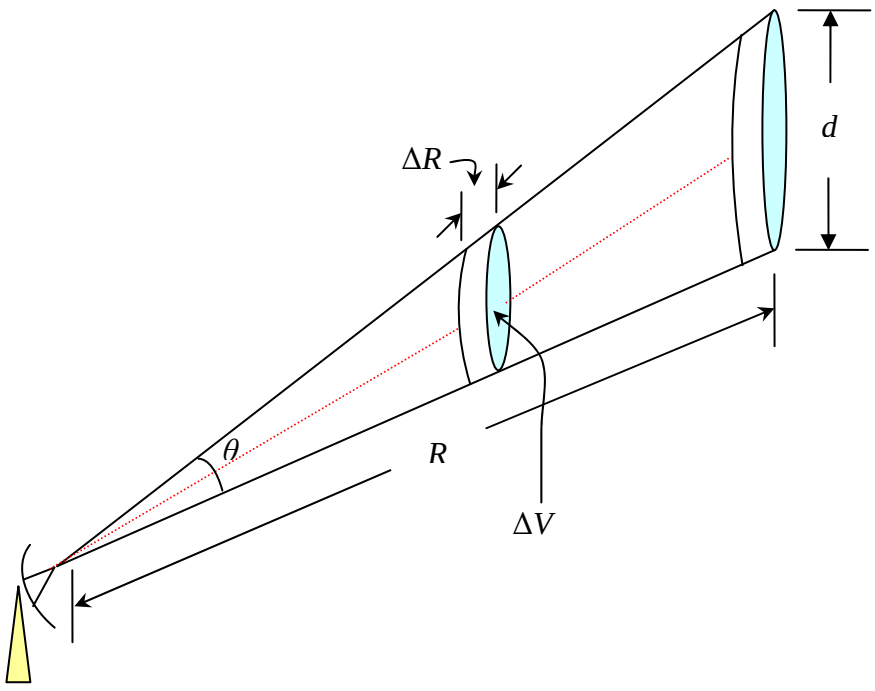

Figure 2-2 Pulsed radar volume resolution for a symmetrical antenna beam.

In section 2.2, we will see that a tradeoff exist between the radar's sensitivity and radial resolution. In practice, there are methods such as pulse compression which present alternatives to overcome this problem. However, it does not apply to our case due to limitations in the signal source.

2.1.2 Receiver

Typically, in pulsed radar applications, a super-heterodyne receiver configuration is used, Figure 2-3. The main feature of a super-heterodyne receiver is to down-convert the received signal from its carrier frequency to an intermediate frequency (IF) which is much easier to process. Initially, the received signal is captured by the antenna and fed to a low noise amplifier (LNA). Later it is fed into a mixer, which combines the carrier signal with another locally generated signal to produce the sum and difference, in frequency, between both. Finally, the upper sideband or "sum", is filtered using a band-pass filter (BPF).

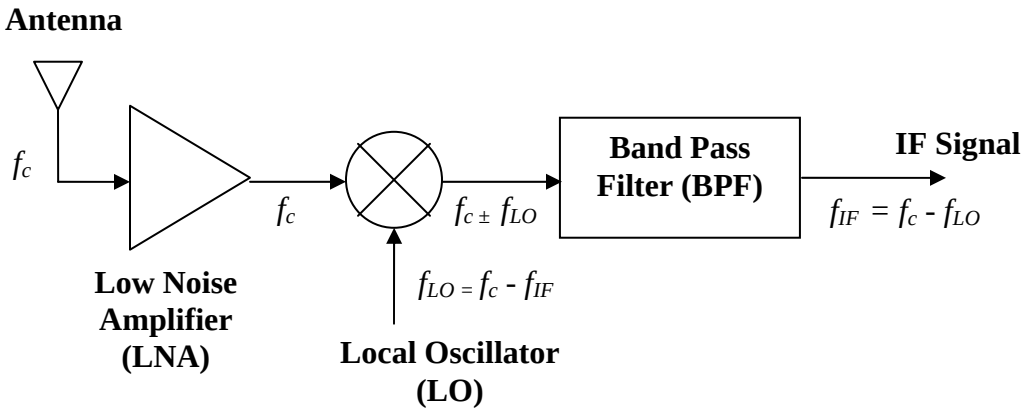

Figure 2-3 Typical super-heterodyne receiver.

In a radar system, the receiver's noise floor determines the lower bound on sensitivity known as minimum detectable signal (MDS). On the other hand, the upper bound is set by the receiver's saturation point also known as its 1dB compression point, Figure 2-4. Basically, these two points make up the dynamic range, Figure 2-4. The dynamic range is defined as the range of signal levels where the receiver's input and output posses a linear relationship.

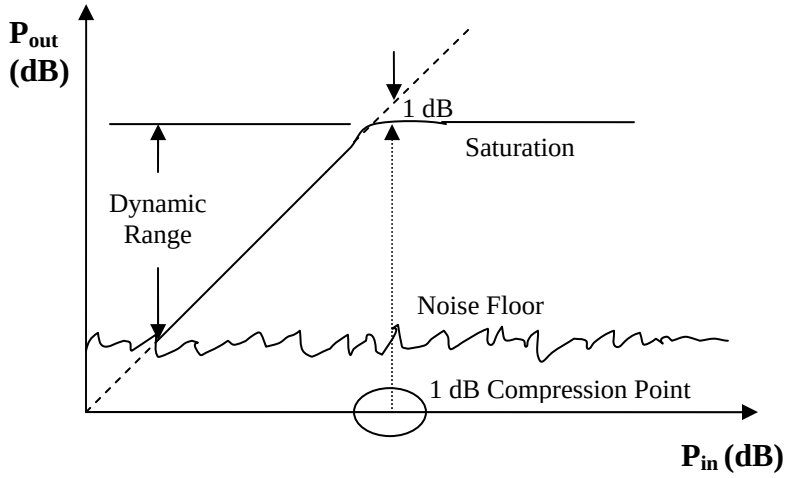

Figure 2-4 Receiver dynamic range example.

Noise power results from random processes such as the movement of charges or holes inside a device, propagation through the ionosphere and/or thermal vibrations of any component having a temperature above absolute zero. Noise in a cascaded system such as radar is calculated using equation 2.3. From equation 2.3, it is noticeable that only the first components, in a cascaded system, make significant noise contributions, and hence why losses need to be kept at a minimum at the initial stages and a LNA is used at the beginning of a radar receiver.

$$F_{sys} = F_1 + \frac{F_2 - 1}{G_1} + \frac{F_3 - 1}{G_1 G_2} + \ldots \quad \textbf{2.3}$$

2.2 Radar Equation

2.2.1 Point Target Radar Equation

If we consider a radar system that uses an isotropic antenna (radiates equally in all directions), we could define the peak power density at any point in space at a range R from the radar as

$$P_D = \frac{P_t}{(4\pi R^2)} \quad \textbf{2.4}$$

where P_t is the peak transmitted power and $4\pi R^2$ is the area of a sphere of radius R. Equation 2.4 represents the hypothetical case of using an isotropic antenna. However, directive antennas are desired in radar systems. Therefore, antenna directivity needs to be taken into account in equation 2.4. This is done in equation 2.6 where G denotes antenna gain. An efficiency of 1, denoted by η, is used and therefore both the antenna gain and directivity (D) are used interchangeably, see equation 2.5.

$$G = \eta D \quad \textbf{2.5}$$

$$P_D = \frac{P_t G}{4\pi R^2} \quad \textbf{2.6}$$

So far, we've determined the power density at a given point in space at a range R from the radar. However, we still need to determine the power received when the radiated

energy impinges on a target and is radiated back. For this, we will define what is called the radar cross section (RCS) as

$$\sigma = \frac{P_i}{P_D}\ m^2 \qquad \textbf{2.7}$$

$$A_e = \frac{G\lambda^2}{4\pi} \qquad \textbf{2.8}$$

where P_i is the power reflected from the target. Finally, squaring the denominator in 2.6, to account for two-way propagation, and multiplying by the RCS and the antenna's effective area (A_e) defined in 2.8, we get

$$P_r = \frac{P_t G^2 \lambda^2 \sigma}{(4\pi)^3 R^4} \qquad \textbf{2.9}$$

where P_r is the power delivered to the receiver by the antenna and λ is the wavelength. Equation 2.8 is called the point target radar equation since it relates the transmitted power to the received power when a radiated wave reflects from a point target.

2.2.2 Distributed Target Radar Equation

Since our application is weather radar, we must go over the case of backscattering by a distributed target. When studying rain events, the total average power received is composed of individual backscatter from hydrometeors within the radar volume, see Figure 2-2 for radar volume. Now, basing ourselves on 2.9 and the following presumptions:

1. The radar volume is completely filled with targets.
2. Multiple scattering is ignored.

3. Total average power is equal to the sum of individual backscattered power.

we can develop the distributed target radar equation.

First equation 2.9 is rewritten for individual targets as

$$\overline{P_r} = \frac{P_t G^2 \lambda^2}{(4\pi)^3} \sum_i \frac{\sigma_i}{R_i^4} \quad \textbf{2.10}$$

where the sum represents the total RCS divided by the individual range to each target within the volume. If we presume $\Delta R << R_i$ than we can rewrite 2.10 as

$$\overline{P_r} = \frac{P_t G^2 \lambda^2}{(4\pi)^3 R^4} \sum_i \sigma_i \quad \textbf{2.11}$$

Now, if we sum the backscattering RCS's over a unit volume of the total radar volume (2.12) we end up with 2.13.

$$\sum_i \sigma_i = \left(\sum_i \frac{\sigma_i}{UnitVolume} \right) * TotalVolume = \left(\sum_i \frac{\sigma_i}{UnitVolume} \right) \left(\frac{\pi R^2 \theta^2 c\tau}{8} \right) \quad \textbf{2.12}$$

$$\overline{P_r} = \frac{P_t G^2 \lambda^2 \theta^2 c\tau}{512\pi^2 R^2} \sum_i \sigma_i \quad \textbf{2.13}$$

Notice the difference in range dependence when observing a distributed target instead of a point target. In the next section, radar reflectivity will be introduced and finally the weather radar equation will be developed.

2.2.3 Weather Radar Equation

Up to now, we have revised both the point and distributed radar equations. Now the weather radar equation is discussed. First, we will introduce a correction needed when

making volume measurements. As proposed by Probert-Jones in [12], the correction factor, term in parenthesis in 2.14, is based on the presumption that the antenna's beam is symmetrical circularly and is approximated by a Gaussian shape.

$$\overline{P_r} = \frac{P_t G^2 \lambda^2 \theta^2 c\tau}{512\pi^2 R^2}\left(\frac{1}{2\ln 2}\right)\sum_i \sigma_i \qquad \textbf{2.14}$$

On the other hand, the sum of all backscattering RCS's per unit volume, third term in 2.14, is defined as radar reflectivity, and represented by the Greek letter η. In the Rayleigh regime, the individual RCS (σ_i) is written as

$$\sigma_i = \frac{\pi^5 |K_w|^2 D_i^{\,6}}{\lambda^4} \qquad \textbf{2.15}$$

so 2.14 becomes,

$$\overline{P_r} = \frac{P_t G^2 \lambda^2 \theta^2 c\tau}{1024(\ln 2)\pi^2 R^2}\left(\frac{\pi^5 |K_w|^2}{\lambda^4}\right)\sum_i D_i^{\,6} \qquad \textbf{2.16}$$

where K_w is the complex dielectric factor for water and D_i is the diameter of the hydrometeors. From 2.16, it is clear that the total average power received has a strong dependence on the target's size. For weather radar, the reflectivity factor Z is defined as [13]

$$Z = \sum_i \frac{D_i^{\,6}}{UnitVolume} \qquad \textbf{2.17}$$

and therefore, 2.16 becomes

$$\overline{P_r} = \frac{P_t G^2 \theta^2 \pi^3 \tau |K_w|^2 Z}{1024(\ln 2) R^2 \lambda^2} \qquad \textbf{2.18}$$

which is known as the weather radar equation.

3 SYSTEM DESIGN

3.1 Introduction

Radar operation at X-band makes the design more cost-efficient than S-band since mature technology for X-band marine radars such as the Raytheon MK2 is commercially available. Another advantage is that component size is inversely proportional to its operating frequency. Therefore, at X-band, components are smaller when compared to others at lower frequencies.

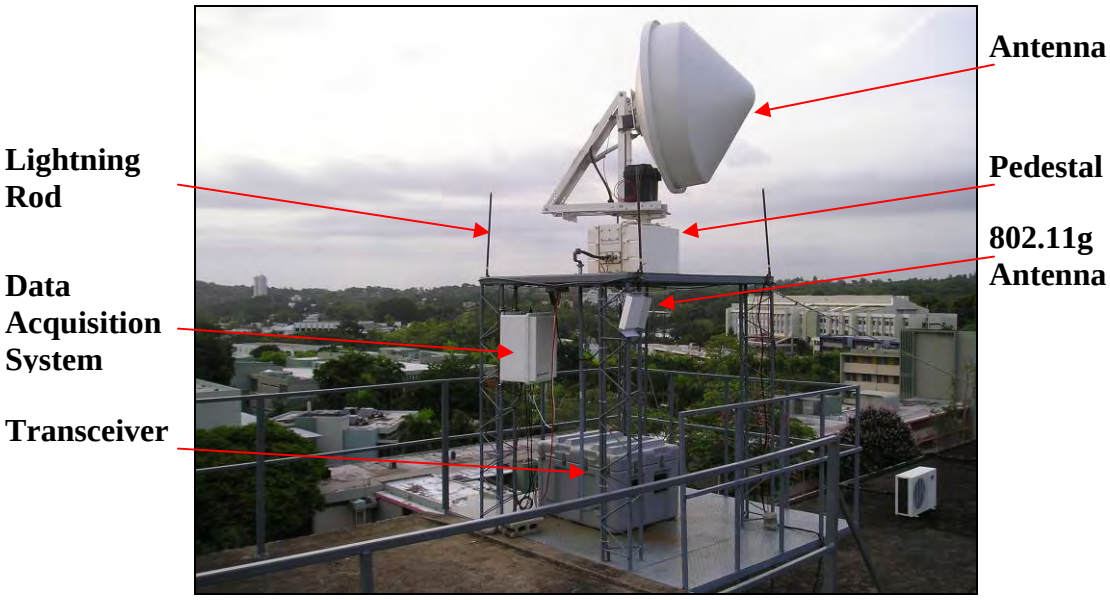

Figure 3-1 CASA STB's PR1.

PR1 consists of a modified Raytheon MK2 “High Seas” marine X-band radar, see Figure 3-1. Modifications to convert the latter into a meteorological radar consisted of replacing the antenna, modifying the antenna pedestal, adding an internal calibration channel (shown in Figure 3-6), replacing the data acquisition system and adding a timer/counter digital I/O module to generate the timing signals. The following sections will describe site planning, the expected sensitivity analysis and all modified subsystems.

3.2 Site Planning

The site survey for the sensing nodes was performed based on both geological and sociological data [14]. By combining both, radar sites that meet the requirements for optimal coverage as well as sociological impact were identified. In the selection process, demographic data from the 2000 US Census of Population and Housing was combined with flooding data from the US Army Corps of Engineers using ArcMap 9.0 [14]. For convenience, PR1 has been installed on top of the ECE building at UPRM. Figure 3-2 shows the chosen radar sites, including PR1.

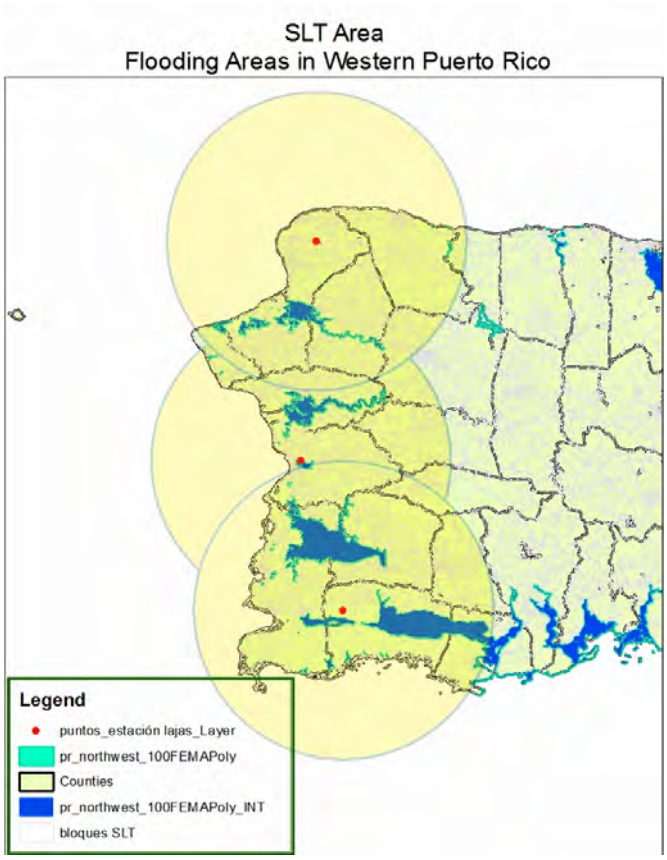

Figure 3-2 Aguadilla, Mayagüez and Lajas node locations.

3.3 Sensitivity Analysis

To estimate the radar's single pulse sensitivity, a plot of the radar's signal to noise ratio (SNR) as a function of range was generated. The system noise floor, shown in Table I as MDS, was calculated using

$$N_i = k\left[T_A + \left(F_{sys} - 1\right)T_0\right]B_{sys} \qquad \textbf{3.1}$$

where k is Boltzmann's constant, T_A is the presumed antenna temperature (200 K), F_{sys} is the system's noise figure calculated using equation 2.3, T_0 is the ambient temperature and B_{sys} is the system bandwidth [15]. Now, Figure 3-3 shows the SNR, in dB, as a function of range, using equation 3.2, which is a scaled version of equation 2.18 [13], to estimate the expected power received. Two relations were presumed to generate this plot. One was the Rosenfeld tropical Z-R relationship [16], which was used to estimate the reflectivity for various rain rates and the other was a k-R (specific attenuation-rain rate) relationship [6], which provided a specific attenuation estimate in (dB/km) for the rain rates used.

Table 1 PR1 system parameters

Carrier Frequency	**F**	9.41 GHz
Wavelength	**λ**	31.88 mm
Peak Power	$\mathbf{P_t}$	25 kW
Antenna HPBW	**θ**	2˚
Antenna Gain	**G**	38.25 dB
Range Resolution	**ΔR**	150 m
Noise Figure	$\mathbf{F_{Sys}}$	8.62 dB
Receiver Bandwidth	$\mathbf{B_{Sys}}$	5 MHz
Minimum Detectable Signal	**MDS**	-98 dBm
1dB Compression Point	$\mathbf{P_{1dB}}$	-8 dBm
Pulse Repetition Frequency	**PRF**	1 kHz
Maximum Range	**R**	~25 km

$$\overline{\Pr} = \left(\frac{\pi^5 10^{-17} P_t(W) G^2 \tau(us) L^2 \theta(\deg) \phi(\deg) |K_W|^2 Z}{6.75 \times 2^{14} (\ln 2) R^2(km) \lambda^2(cm)} \right) \quad \textbf{3.2}$$

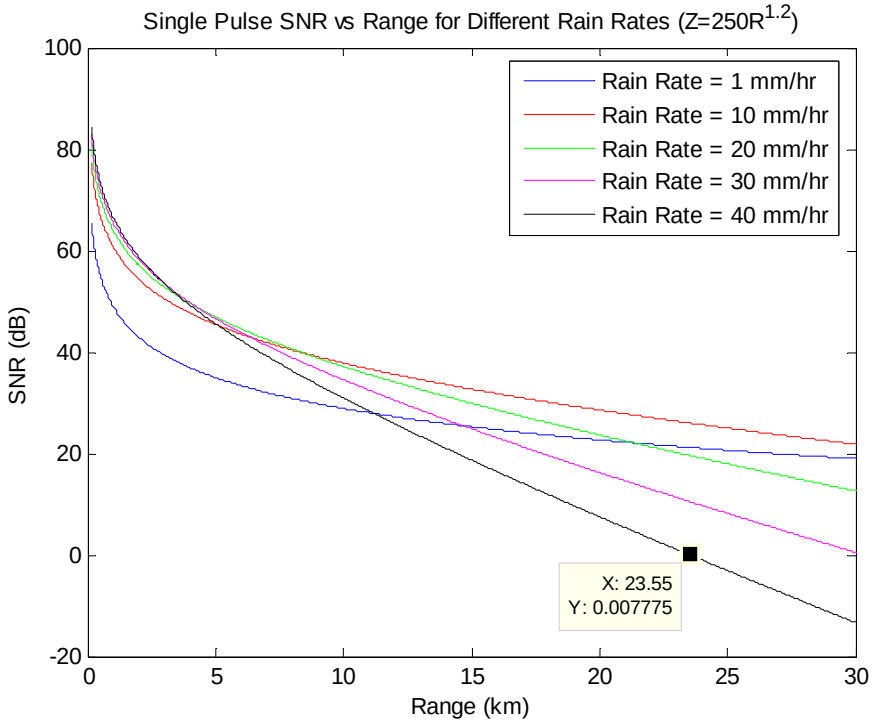

Figure 3-3 SNR vs. range at various rain rates.

From Figure 3-3, we can see that for a SNR of 0 dB during a worst case scenario of 40mm/hr rain rate across the entire path, our maximum detection range would be approximately 24 km. However, using non-coherent pulse integration, a 17 dB improvement in SNR is achieved which in turn translates into a probability of detection of 0.99 and a false alarm probability of 10^{-12} [17] [18]. Therefore, the required 25km range for PR1 should be feasible.

3.4 Modifications

3.4.1 Antenna

The Raytheon MK2 “High Seas” X-band marine radar system has three antenna options. These are 6, 7 and 9 feet linear arrays. Basic antenna parameters for these systems are 1.2 to 0.9 horizontal and 25 to 23 degree vertical beamwidths. Gains for these antennas range from 29 to 30dB. The major drawback of these type of antennas is their large horizontal beamwidth. This is caused by their small vertical area. In meteorological radar applications this is not acceptable since both the vertical and horizontal resolution are of great importance when scanning the atmosphere. For this reason, the original antenna was replaced.

The new antenna, shown in Figure 3-4, was built by Seavy Associates. It is a parabolic reflector antenna. Table 2 summarizes its main parameters.

Table 2 PR1 antenna parameters

Antenna Parameter	H-Plane	E-Plane
Gain (dBi)	38.25	
HPBW	2.0	1.75
First Side Lobe (dB)	19.9	16.0
Cross-Pol Level (dB)	41.0	

From Table 2, it is noticeable that the antenna has dual polarization capabilities. This is achieved by an ortho-mode transducer (OMT) built into the antenna's feed. Although PR1 is currently a single polarization system, future plans are to remodify it into a dual polarization radar. Making PR1 dual-pol will introduce other rain estimators currently being used in the radar community. Another advantage of the new antenna is its higher gain. This is a major factor in achieving PR1's sensitivity, see equation 3.2.

Figure 3-4 PR1 Antenna and pedestal.

On the other hand, the antenna pedestal has angular velocity of 24 RPM. Now, from a meteorological radar perspective, having a high antenna angular velocity is good since it translates into smaller full-scan times. However, this means, higher PRF's are needed to achieve the desired sensitivity since we are relying on pulse integration for this matter.

PR1's magnetron has a maximum duty cyle of 0.001, which sets our maximum PRF to 1 kHz if a 150 m (τ = 1 us) radial resolution is desired. With this configuration we could only integrate 13 pulses. Now, our sensitivity analysis was based on integrating 100 pulses. Therefore the antenna pedestal's angular velocity was brought down to approximately 3 RPM, which gives us 111 pulses for integratrion.

Modifications to the antenna pedestal, shown in Figure 3-5, were performed at the Physic's building machine shop. These included adding a plate to mount extra pulleys to reduce its angular velocity.

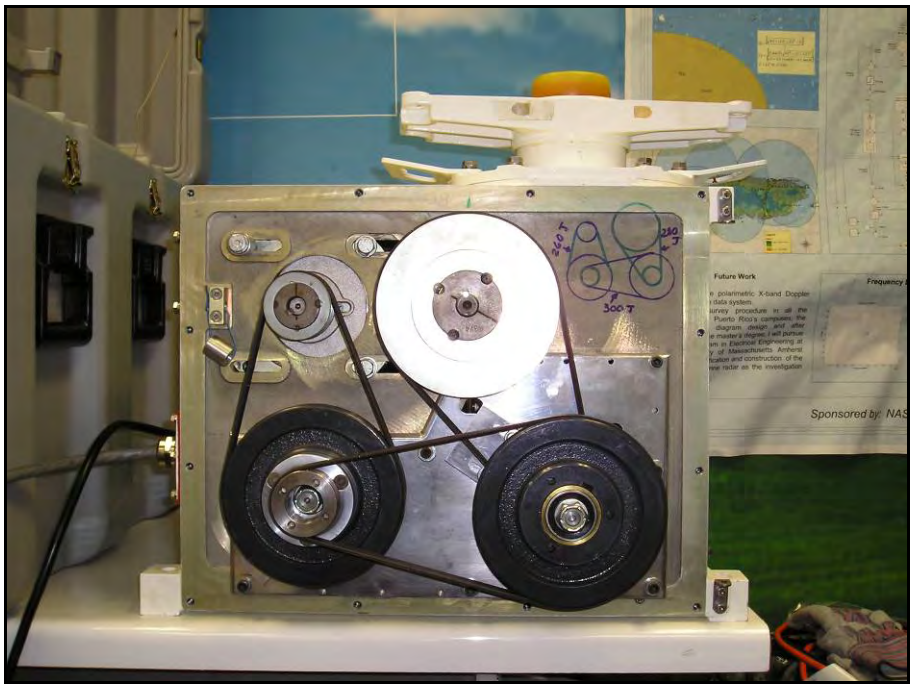

Figure 3-5 Modified antenna pedestal.

3.4.2 Calibration Channel

The main purpose of the calibration channel is to measure transmitted power and monitor the receiver's gain [10]. By doing so, better measurements are achieved because variations in these two parameters are caught and accounted for when estimating Z. Receiver noise figure measurements are also possible, however with low accuracy, using the Y-factor method [19].

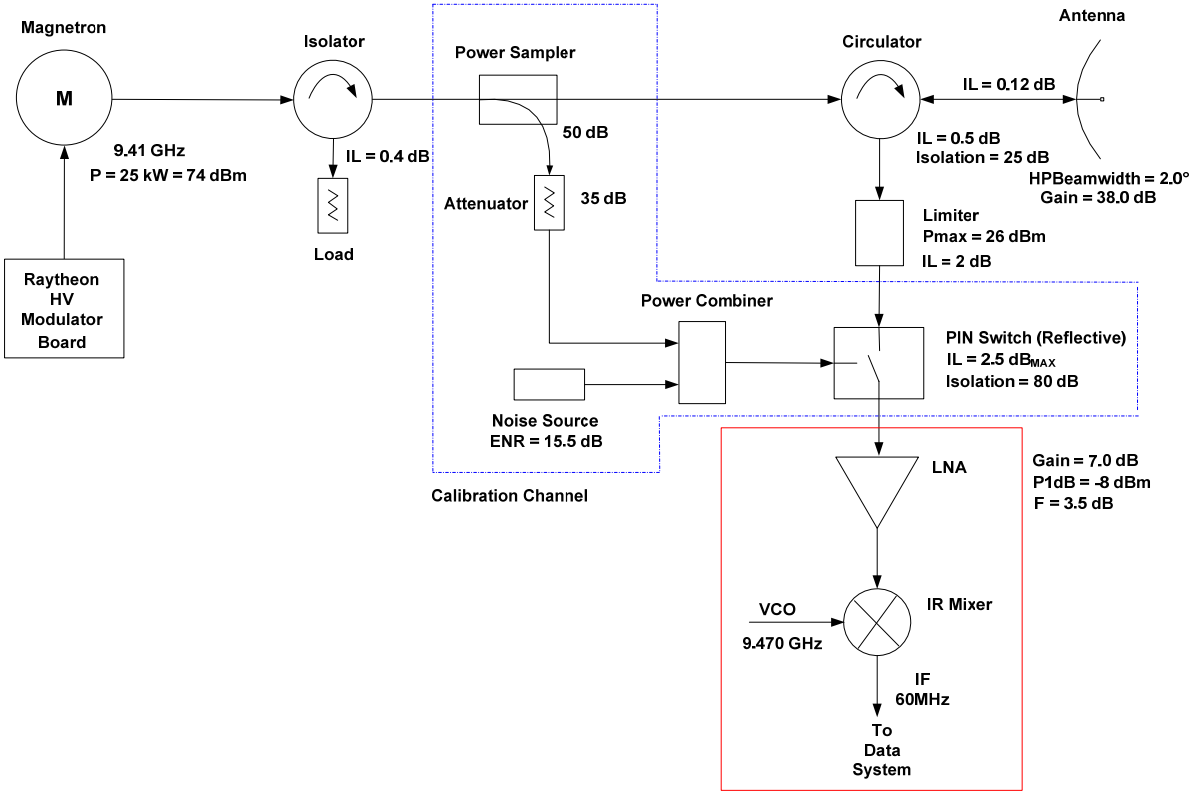

Figure 3-6 Modified RF front-end block diagram.

PR1's calibration channel, shown in Figure 3-6, consists of a 50 dB power sampler, 35 dB attenuator, 15.5 dB ENR noise source, power combiner and a high isolation PIN

switch. To achieve a low calibration error, special consideration was given to the isolation between the transmit leakage and calibration paths. From [10], the needed isolation for a 0.1 dB calibration error is given by

$$e_{cal}(dB) = \left| 20\log_{10}\left(1 - \sqrt{\frac{P_{leak}}{P_{cal}}}\right)\right| \qquad \textbf{3.3}$$

From equation 3.3, it follows that at least 40 dB of isolation is needed between the transmit path leakage power and the calibration power for a 0.1 dB calibration error. See Figure 3-7. PR1 has a 43 dB isolation between transmit leakage and calibration power. Therefore it should have a calibration error lower than 0.1 dB.

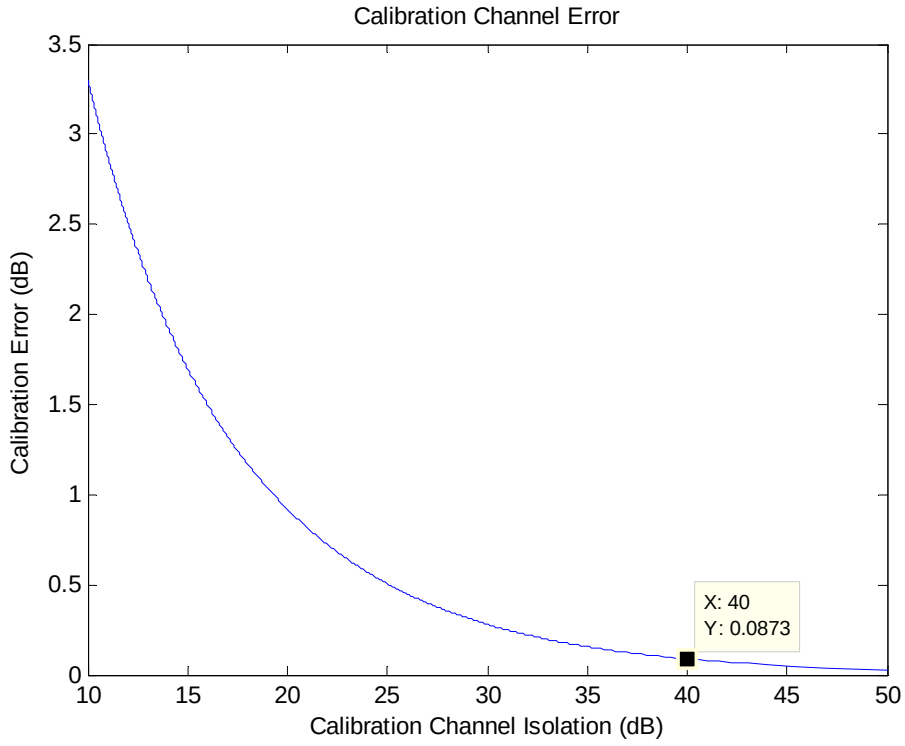

Figure 3-7 Calibration channel error vs. isolation.

3.4.3 Data Acquisition System

Radar control and data acquisition is handled by a Linux based VIA EPIA MII mini ITX embedded PC, see Figure 3-9. It is equipped with an Adlink PCI-8554 counter/timer, PCI-9812 data acquisition card and a PCMCIA wireless card with 802.11g capabilities, see Tables 3 and 4. Trigger signals are generated by the counter/timer card and fed into the high voltage modulator and calibration switch, for transmission and internal calibration respectively. Data from the antenna azimuth optical angle encoder is deciphered and sent through the PCI bus using the PCI-8554 (Figure 3-8), while the video signal from the logarithmic amplifier is sampled by the PCI-9812.

Table 3 PCI-8554 timer/counter board specifications

Counter Devices	Four 82C54 counter/timer chips
Counter/Timers	10 independent counters and one 32-bit counter
Counter Modes	16-bit down counter Binary or BCD
External Clock	10 MHz maximum
Clock Sources	Cascaded 32-bit counter output
	External clock
	Prior counter output
	On-board 8 MHz clock
Digital I/O	8 inputs and 8 outputs - all TTL

On the other hand, a digital inclinometer measures the antenna's elevation angle and transfers it to the embedded PC's serial port through a transparent Bluetooth wireless connection.

Table 4 PCI-9812 data acquisition card specifications

Max. Sampling Rate	20 MSPS
Resolution	12-bits
Input Channels	4 single-ended (BNC)
Input Channel Range	±1 V or ±5 V
Accuracy	Gain error: ± %1.5
Input Impedance	50Ω / 1.25kΩ /15MΩ user select
FIFO Size	8k samples/channel
Trigger Source	Software, external digital and analog
Trigger Mode	Software, pre, post, middle and delay
Data Transfer Mode	DMA
Clock Source	Internal, external digital and analog
Internal Clock Frequency	40MHz / n programmable

Since the magnetron trigger and optical encoder signals are differential, and the I/O of the PCI-8554 is TTL, signal conditioning was needed. Therefore, an interface board, between the transceiver and the embedded PC, was designed to handle all signal conditioning and provide software controllable transceiver and antenna rotation On/Off capabilities using the digital outputs of the PCI-8554 combined with relays. Furthermore, to synchronize the data acquisition with the magnetron trigger, the latter was split inside the interface board and

fed into the PCI-9812. This way the PCI-9812 starts to acquire data every time the magnetron is triggered. See Figure 3-9 for a detailed block diagram of the interface board.

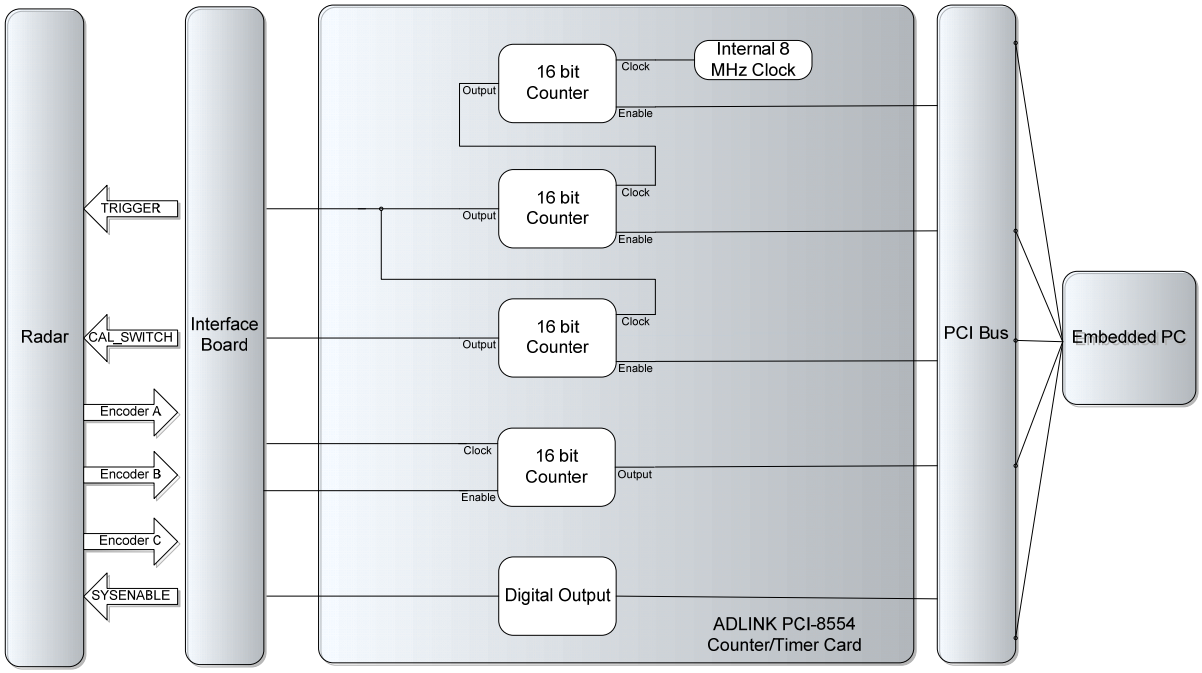

Figure 3-8 PR1 control board and embedded PC.

Currently, all acquired data is locally stored locally as text files and then transferred to a server using the 802.11g wireless card. To minimize data throughput rates, pulse integration takes place inside the embedded PC. This reduces the data size by a factor of as much as 100 times when integrating 100 pulses. Figure 3-11 denotes the data acquisition algorithm which handles the pulse integration. This algorithm, as well as the radar control was all implemented using C code.

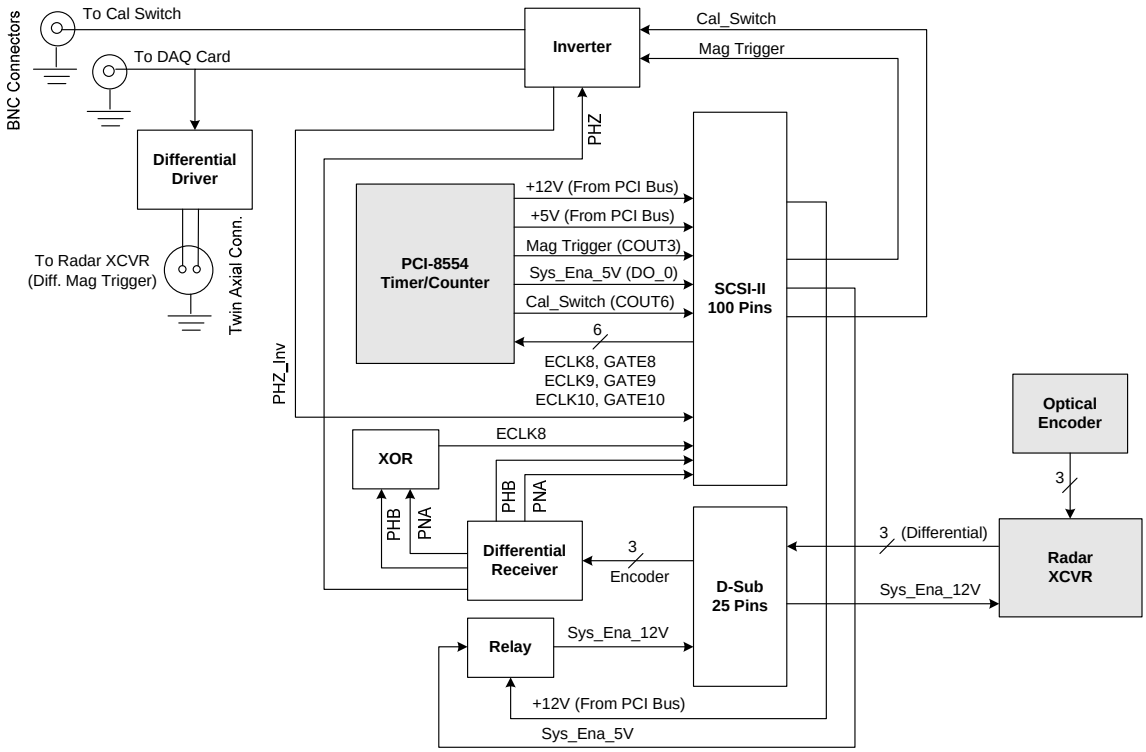

Figure 3-9 PC interface board block diagram.

In the future, data storage and processing will be handled by grid computing algorithms described in [20]. These algorithms will handle the data and make it available to the end users in a transparent manner in NetCDF format. Furthermore, [20] uses the Information Dispersal Algorithm (IDA) to achieve better data reliability with less storage spending when compared with traditional data replication.

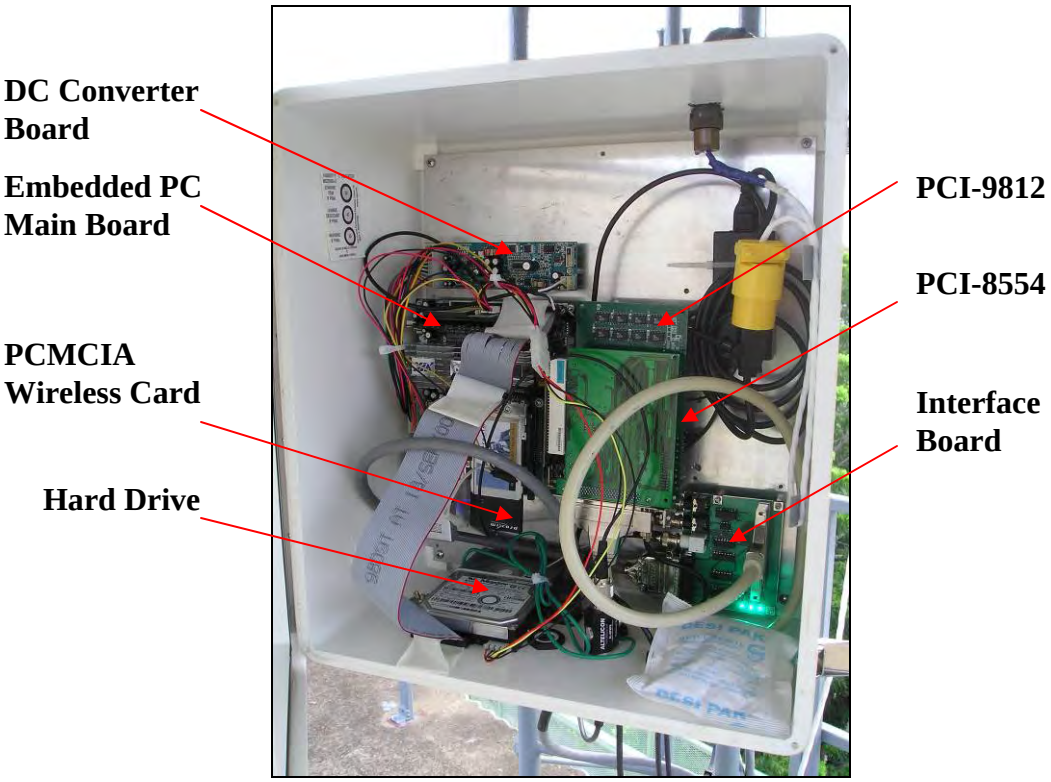

Figure 3-10 PR1's data acquisition system.

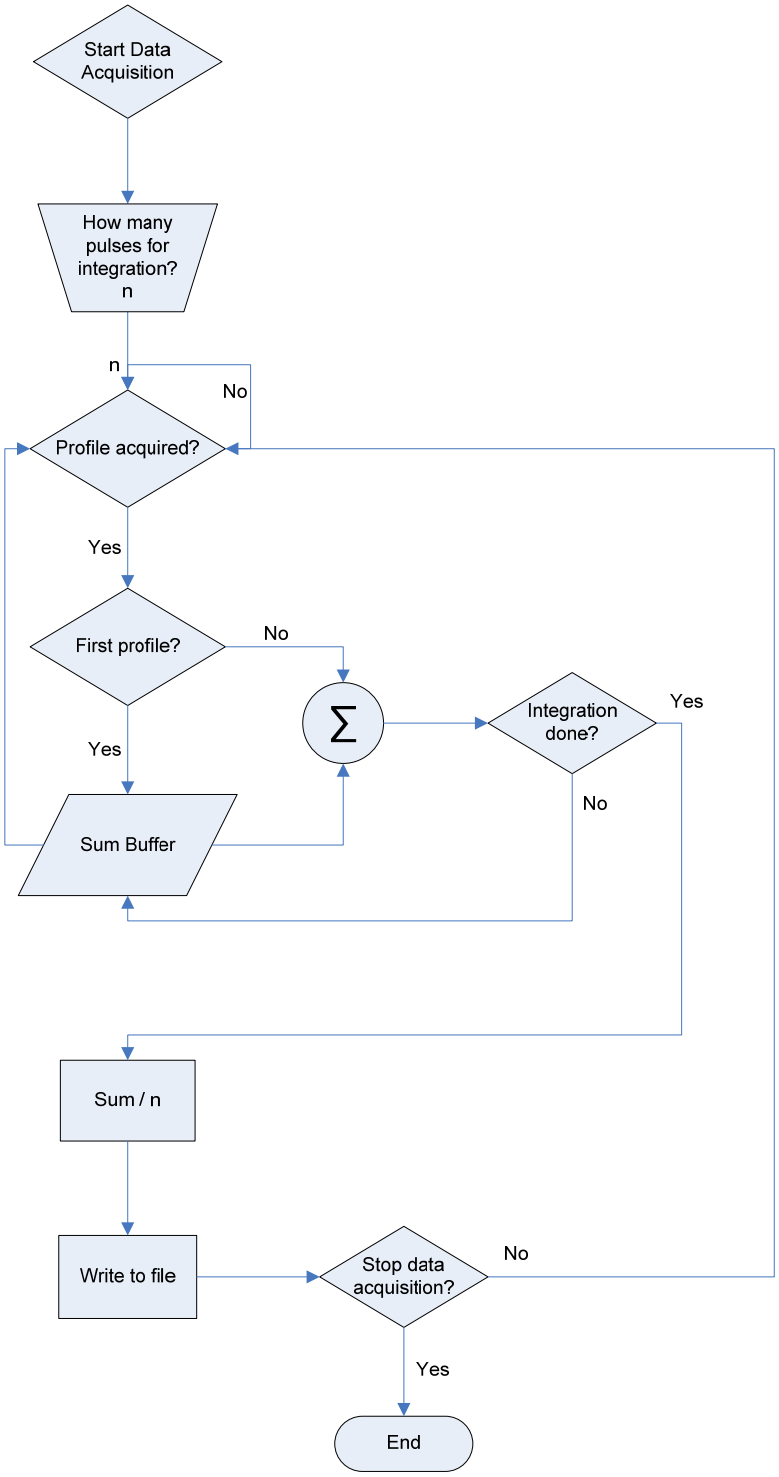

Figure 3-11 PR1 pulse integration algorithm flow chart.

4 CALIBRATION AND INITIAL DATA

4.1 Calibration

4.1.1 Calibration

Following down-conversion to 60 MHz in PR1's receiver, logarithmic detection takes place. The logarithmic amplifier takes the 60 MHz IF input and outputs a DC voltage proportional to the power of the input IF signal. Our particular log-detector has a maximum output voltage of 1.5 V. Therefore, logarithmic detection compresses the entire receiver dynamic range into a 1.5 V_{Max} signal.

To calibrate the receiver, a power sweep from -82dBm to -23dBm, in 2dB steps, using a 9.41 GHz CW signal was injected, into the transceiver input port, while recording the output voltage using an oscilloscope [21]. As a result, the measured voltage should be linear with respect to the input power sweep. Figure 4-1 shows a scatter plot along with a least squares linear fit. The final equation used was

$$V_{Log-Detector} = 1.589 + 0.01580 P_{Received} \qquad \textbf{4.1}$$

where $V_{Log\text{-}Detector}$ is the logarithmic amplifier output voltage and $P_{Received}$ is the power injected into the receiver. From Figure 4-1, it is also noted that the linear fit has an R^2 statistic of 99.8% which suggests it is a good one.

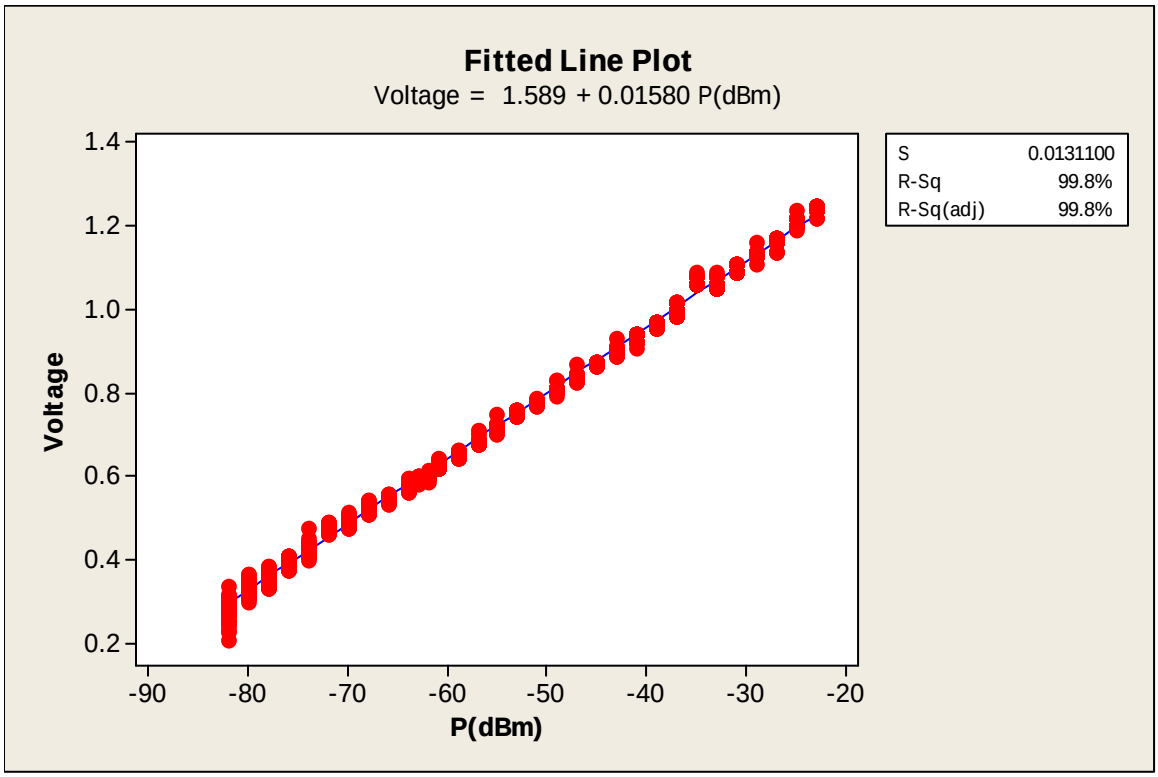

Figure 4-1 Receiver calibration regression.

Now, since the receiver calibration was performed at the transceiver input port, there's a significant part of the system that needs to be accounted for. This is the waveguide connecting the antenna to the transceiver. The insertion loss through the waveguide was measured (0.12dB) and accounted for when generating the reflectivity images. Another loss term included in the reflectivity calculation was the receiver's finite bandwidth loss. From [13], an estimate of this loss was made using

$$lr(dB) = 10\log\left[\left(\coth(aB\tau) - \frac{1}{2\sqrt{\ln 2}}\right)^{-1}\right] \qquad \textbf{4.2}$$

where B is the receiver's bandwidth, τ is the transmitted pulse width and

$$a = \frac{\pi}{2\sqrt{\ln 2}} \qquad \textbf{4.3}$$

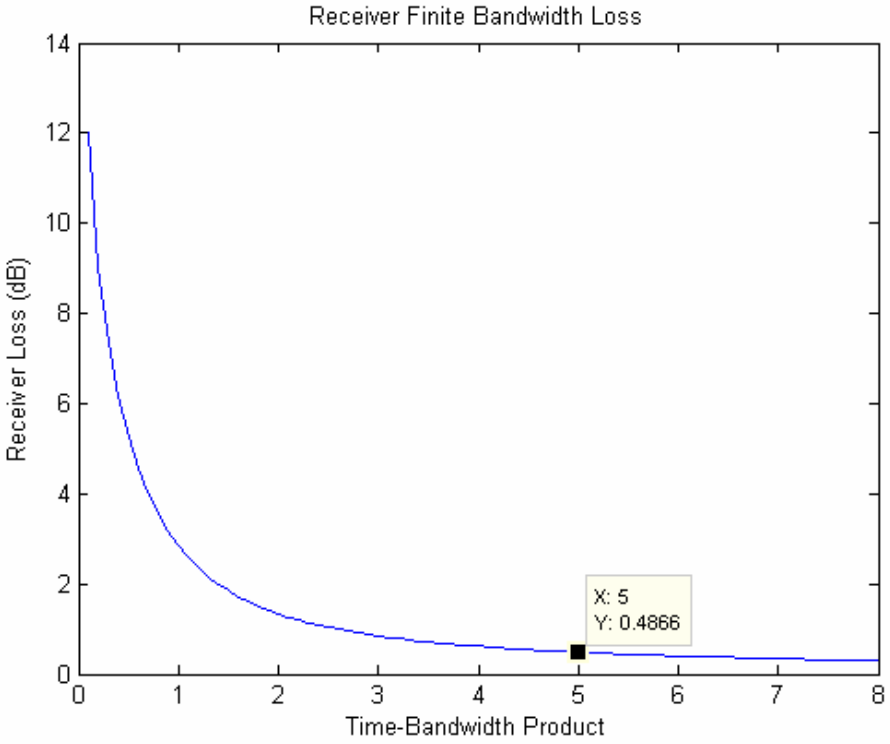

Figure 4-2 Receiver finite bandwidth loss.

From Figure 4-2, we can see that for our case ($B\tau$ = 5) the receiver's finite bandwidth loss is 0.4866dB. Therefore, the remaining losses after calibrating the logarithmic detector sum up to 0.6066dB. This calibration includes the receiver all the way up to the antenna terminals but not the antenna itself neither the transmit path. To calibrate the entire system, a target with a known RCS was used. The type of target used was a trihedral corner reflector with a 1000m^2 RCS.

To prevent receiver saturation and large side lobe clutter contamination, the corner reflector was placed on a cliff at a distance of approximately 6km from the radar. Figure 4-3 shows the expected return power expected using the point target radar equation.

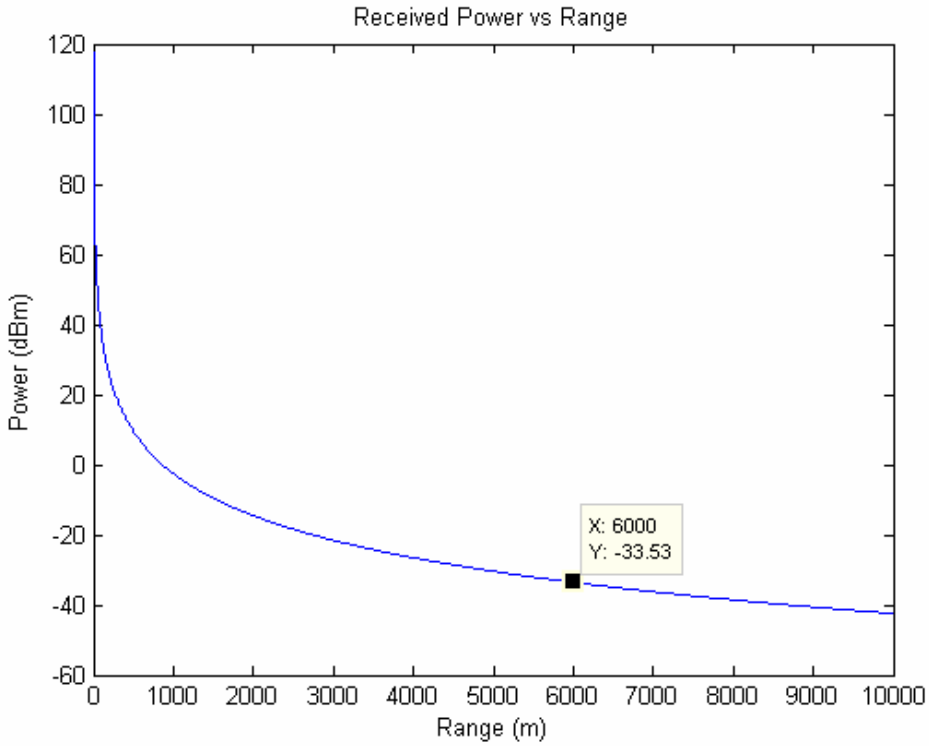

Figure 4-3 Expected received power using 1000m^2 corner reflector.

Although the radar reflector was mounted and aligned with the antenna, no large return was seen at the receiver. This may be caused by an image of the corner being formed on the ground. This image may cause the returned signal to cancel itself. A way to get around this, is to vary the height of the corner reflector, however during our efforts this was not possible. Therefore our calibration relies on the antenna measurements made by the manufacturer. On the transmit side, magnetron power variations were monitored using the internal calibration channel.

4.2 Initial Data

Although data was recorded during other days, July 11th 2007 was chosen to perform an initial validation of the data acquired. In this day, thunderstorms were present during the afternoon. Throughout this section, data from PR1 will be validated using data from Nexrad (TJUA), atmospheric soundings and rain gauge data. Figures 4-5 through 4-11 show the data acquired during the thunderstorms. All images from PR1 were created using the Matlab code shown in appendix A and were then overlaid using Google Earth.

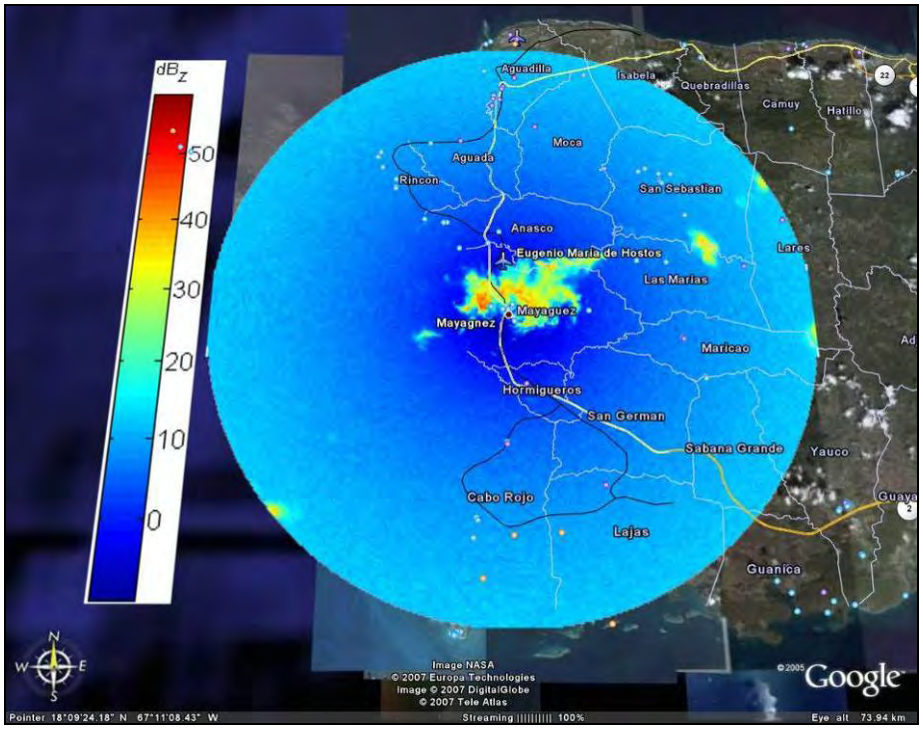

Figure 4-4 071107-130312_PR1.dat

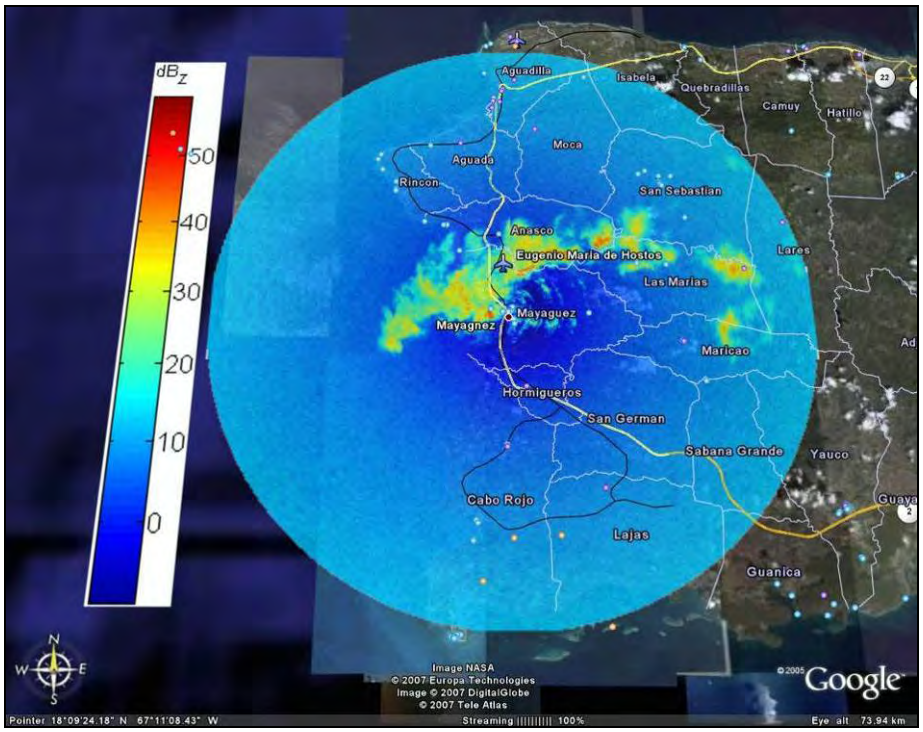

Figure 4-5 071107-132339_PR1.dat

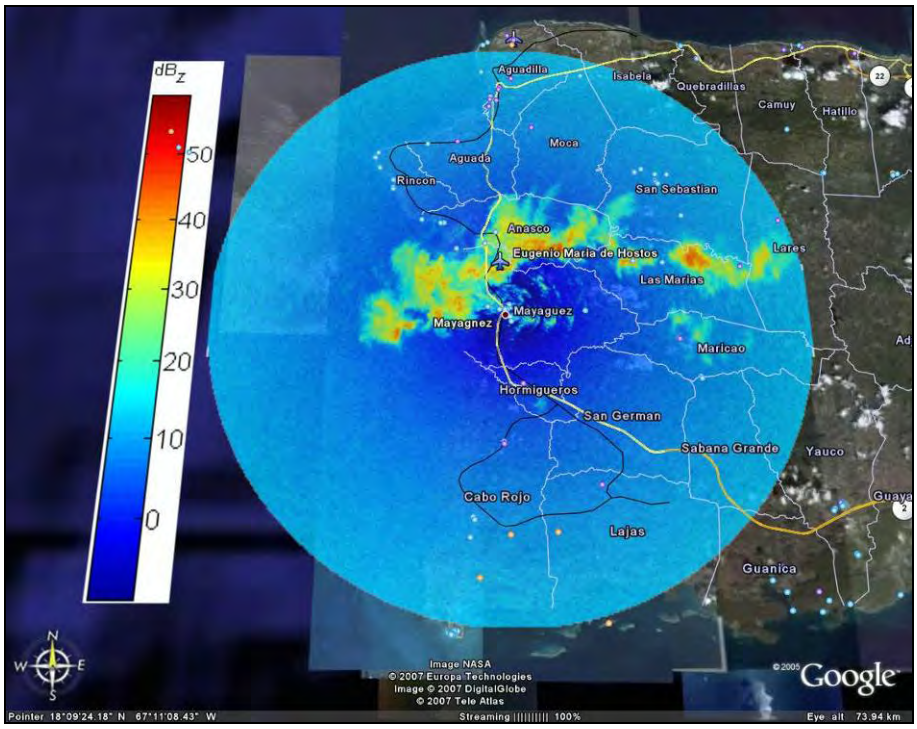

Figure 4-6 071107-133032_PR1.dat

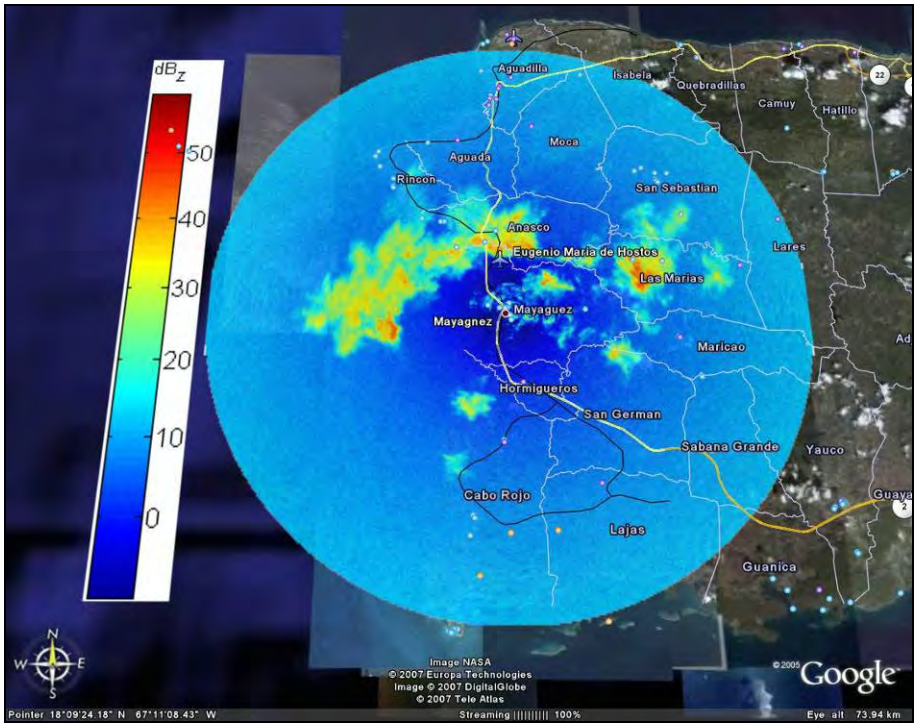

Figure 4-7 071107-134358_PR1.dat

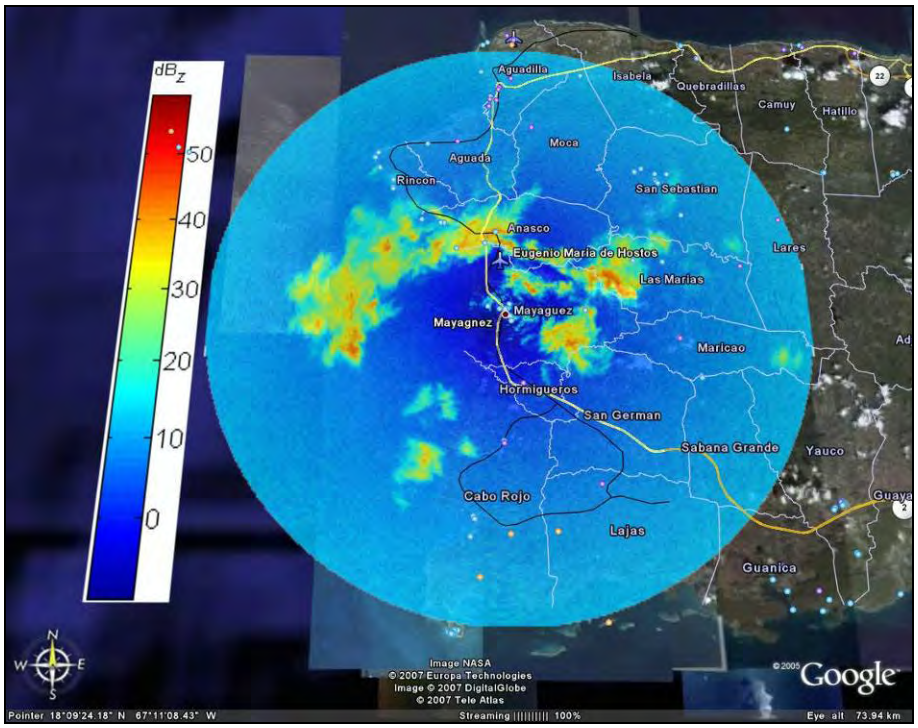

Figure 4-8 071107-135146_PR1.dat

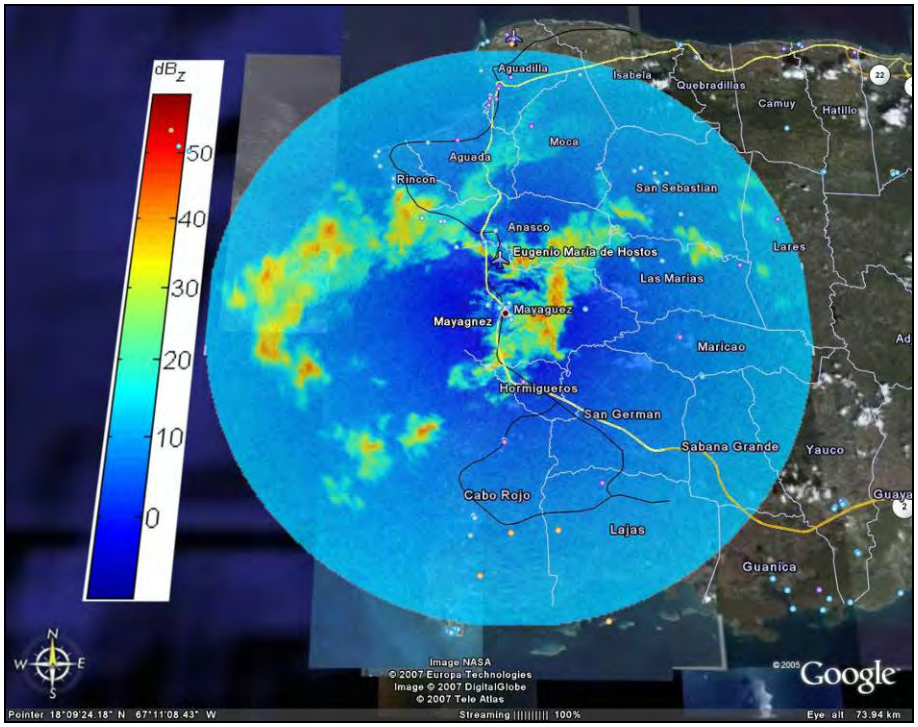

Figure 4-9 071107-140621_PR1.dat

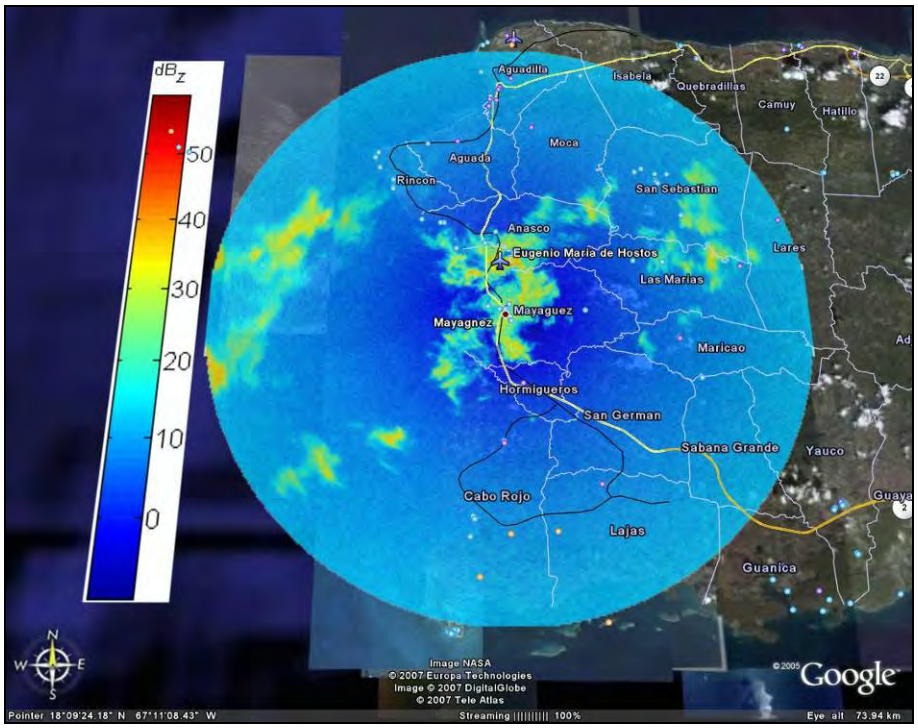

Figure 4-10 071107-141938_PR1.dat

From Figures 4-5 through 4-11 it's noticeable that the thunderstorms formed at the western part of the island and moved toward the west. This is in agreement with the atmospheric soundings from San Juan at 0 and 12 UTC [22]. Figures 4-12 and 4-13 show the skew-T diagrams of the soundings performed this day. In both soundings, it's noticeable the winds were blowing from the east at approximately 15 to 20 knots.

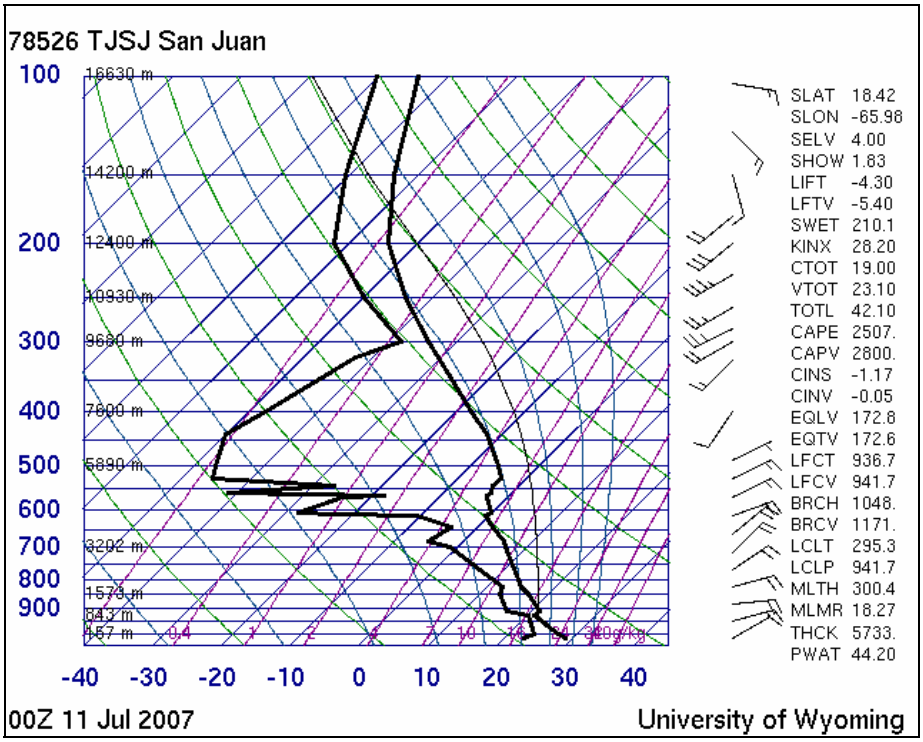

Figure 4-11 Atmospheric sounding done on July 11th 2007 by the NWS.

Also from both soundings, but especially from the first one, Figure 4-11, the CAPE index was high [22]. CAPE stands for Convective Available Potential Energy. It represents the amount of buoyant energy available to accelerate a parcel vertically. The higher the CAPE value is, the more energy is available to foster storm growth [23]. Values from 1000 to 2500 suggest moderately unstable conditions while values higher than 2500 represent very

unstable conditions [23]. While the soundings were upwind of Mayaguez at San Juan, the CAPE index values on July 11 were quite high, 2507 and 1874. This demonstrates that there was potential for strong convection during this day, which agrees with the images from PR1 [22].

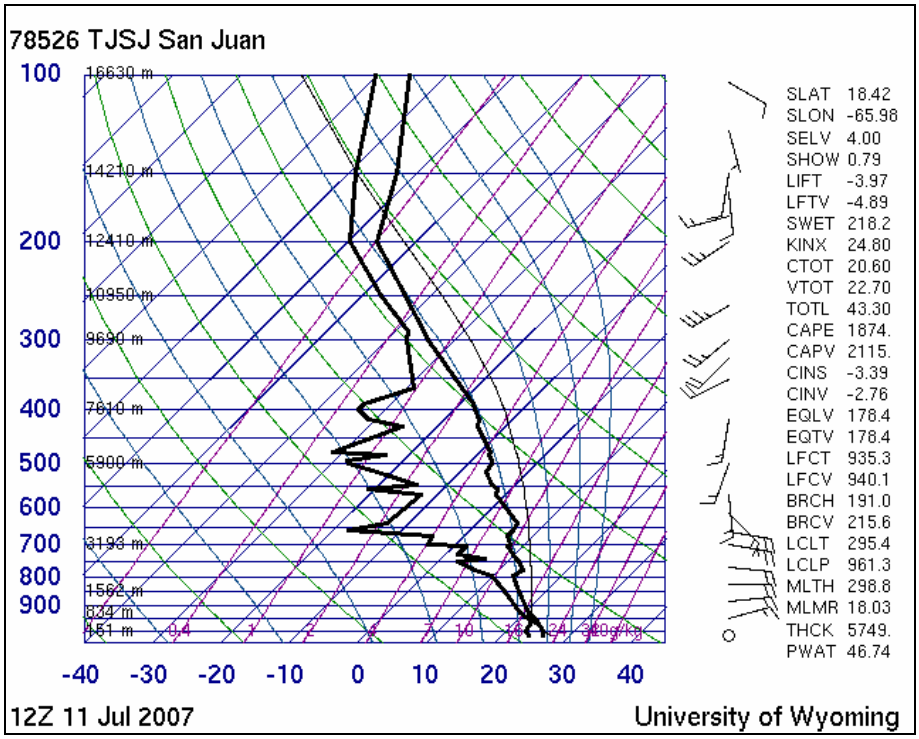

Figure 4-12 Atmospheric sounding done on July 11th 2007 by the NWS.

Figures 4-13 and 4-15 are level II data images of Nexrad paired up with the corresponding PR1 images. The first thing we should note is the low resolution of the rain regions in the Nexrad images. This is caused by the increase of the radar pulse volume size with increasing range. The San Juan radar is over 100 km from Mayagüez and this means that the radar volumes are about 2 km in the azimuthal direction. Another possible issue that may have caused differences in the data is that both systems are not time synchronized.

Therefore, data was not being collected exactly the same time and storms may have moved or their features changed during this time difference. Differences in time, in the data shown, are in the order of minutes.

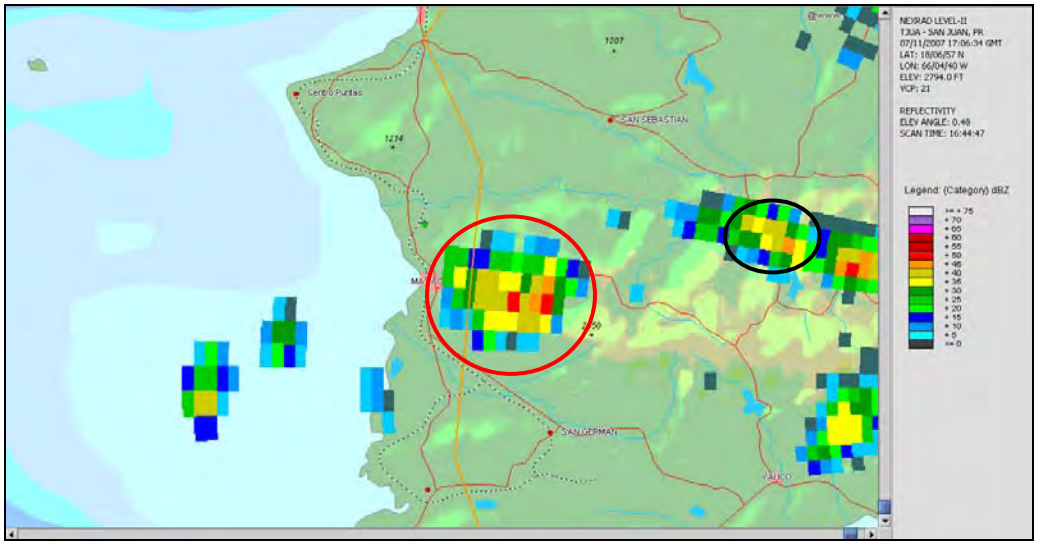

Figure 4-13 Nexrad data – 07/11/2007 13:06:34 local time.

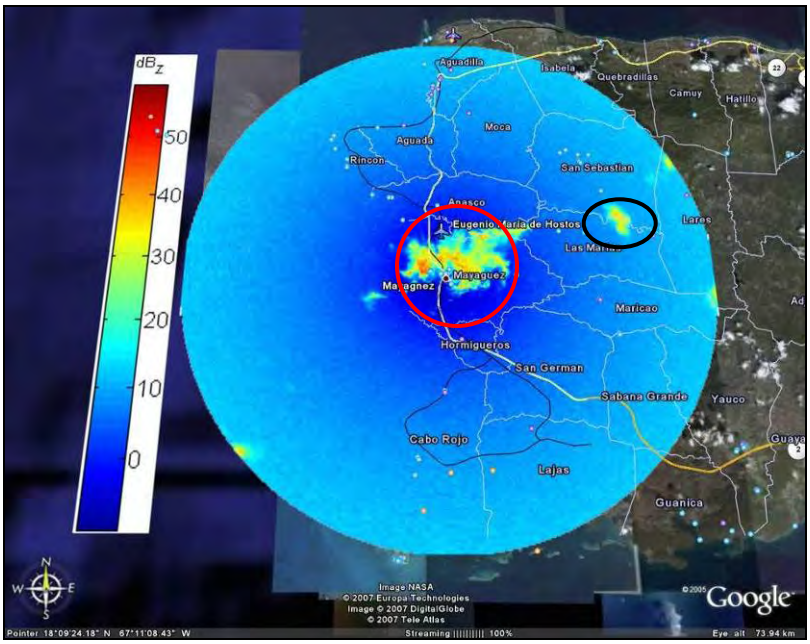

Figure 4-14 PR1 data - 07/11/2007 13:03:12 local time.

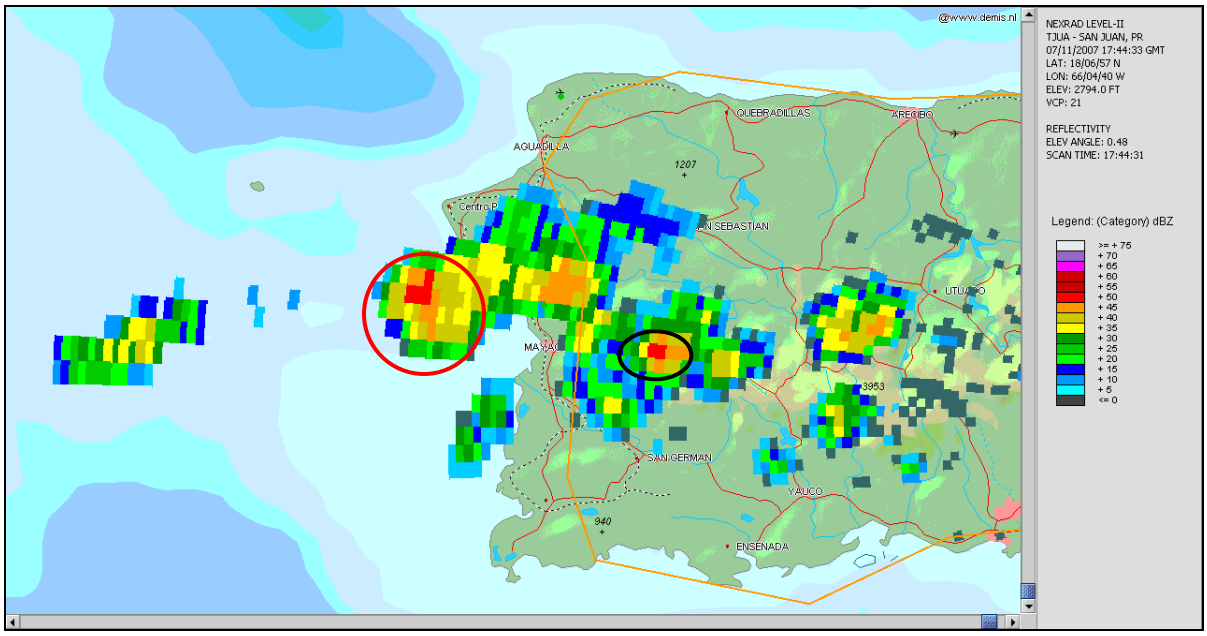

Figure 4-15 Nexrad data - 13:44:33 local time.

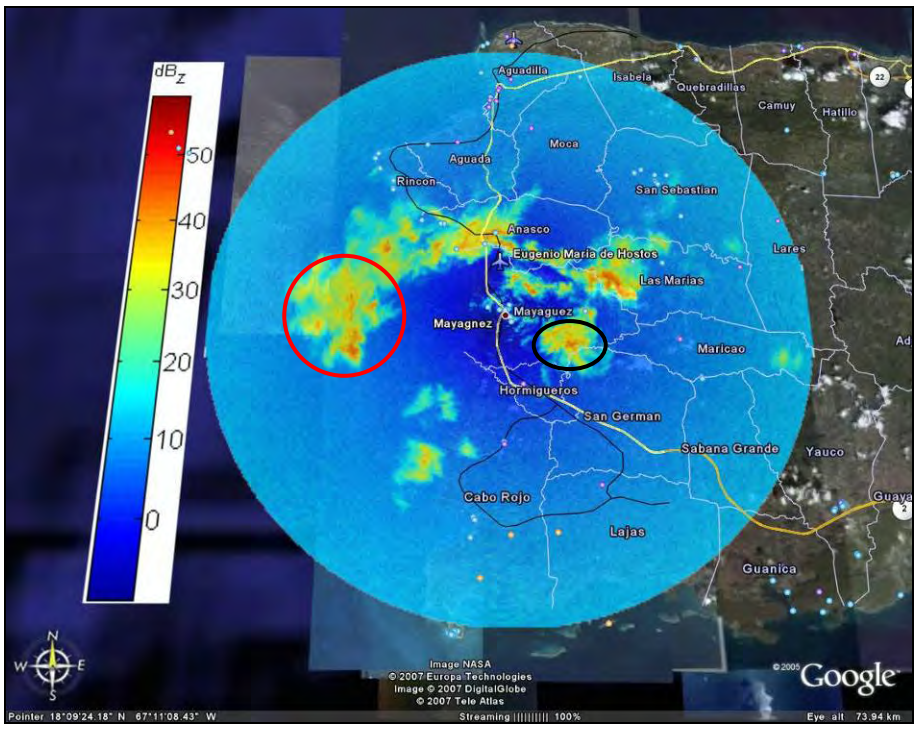

Figure 4-16 PR1 data - 07/11/2007 13:43:58.

Corresponding red and black circles in the image pairs show the common areas where both radar systems had some similarities. These similarities confirm that there was weather activity at the same locations during the time span chosen. Furthermore, it is noticed that PR1's images show a higher level of detail regarding the features of the weather detected. This is mainly because of its higher resolution.

The final data validation was performed using data from a rain gauge network composed of 12 sensors located in Barrio Miradero, Mayagüez. Figure 4-17 shows the network along with data from July 11, 2007 at 14:06.

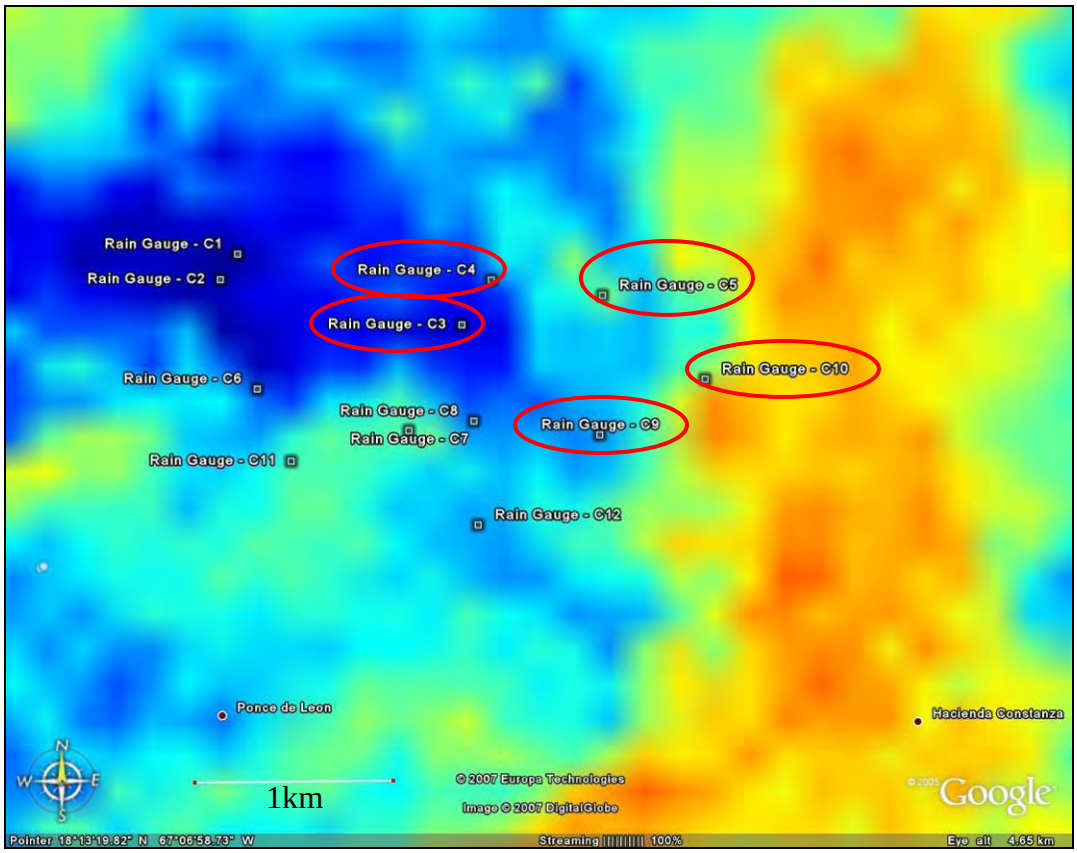

Figure 4-17 Miradero rain gauge network.

Table 5 Miradero rain gauge network data from July 11th 2007

Rain Gauge	Rain Rate (mm/h)
C1	6.1
C2	3.0
C3	54.9
C4	58.9
C5	48.8
C6	15.2
C7	12.7
C8	18.3
C9	57.9
C10	39.6
C11	0
C12	3.0

Highlighted values in Table 5 show the highest rain rates measured. These rain gauges are circled in red in Figure 4-17. Rain gauges C5, C9 and C10 support the radar data since they're the ones closest to the high reflectivity region. However, sensors C3 and C4, which have the highest readings, are not located within high reflectivity regions. Once again, time synchronization or even mapping problems

might be causing disagreement between the Miradero rain gauge network data and PR1's.

5 CONCLUSIONS AND FUTURE WORK

The main objectives of this research were met successfully. These were, to develop the first node of CASA STB's X-band short range radar network and perform initial data comparison using Nexrad data.

To complete the radar design, implementation and testing within the two-year time frame, the design was based on a commercially available marine radar system (Raytheon MK2). Although a very similar design approach was used at UMass, this work has its own unique features, and most importantly, this type of system has never before been developed at UPRM. Therefore, the success of this research has raised the level of competence, in radar design, at UPRM. This will have a positive impact in winning new radar related proposals in the future. Some features that differentiate PR1 from other systems are its modified antenna pedestal, the data acquisition system configuration, its internal calibration channel configuration and wireless data transmission.

Now, regarding the initial data, when compared to Nexrad and the Miradero rain gauge network, and combined with the atmospheric soundings, it shows that PR1 was making true measurements. The differences observed in the comparison could have been caused primarily by time differences and possible mapping errors. Furthermore, it's very clear that PR1 has greater volume resolution (more than 6 times), which highlights weather features not captured before by Nexrad. This will enhance the study of weather events in

western Puerto Rico. The Nexrad data comparison performed is the first ever performed in western Puerto Rico using locally acquired data using an X-band radar.

On the other hand, this work has helped lay down the ground work for further studies/radar development at UPRM. PR1 still needs to be thoroughly validated before it can be used by the National Weather Service in San Juan. After being carefully validated, attenuation studies in a tropical environment could be performed as well as QPE measurements. Further work in upgrading PR1 to a Doppler radar would also contribute greatly since wind measurements are also of importance in weather prediction. Dual polarization measurements may be justified by the attenuation studies and therefore require PR1 be upgraded to have this capability. Hence, PR1 has provided new opportunities for other students to develop radar skills while undergoing studies at UPRM.

REFERENCES

[1] Collaborative Adaptive Sensing of the Atmosphere (CASA) Engineering Research Center, "Overview" [Online]. Available from http://www.casa.umass.edu, 2003.

[2] Vega, M.A., Colom, J., "Student Developed Meteorological Radar Network for the Western Part of Puerto Rico: First Node", *IEEE Transactions on Geoscience and Remote Sensing* , July 2007.

[3] Trabal, J., Puerto Rico Deployable Radar Network Design; Site Survey and Radar Design., M.S. Thesis, University of Puerto Rico at Mayagüez, December 2003.

[4] Rollenbeck, R., Bendix, J., "Experimental calibration of a Cost-Effective X-Band Weather Radar for Climate Ecological Studies in Southern Ecuador", *Elsevier Atmospheric Reasearch*, No. 79, pp. 296-316, June 2005.

[5] Galati, G., et. al., "Digitalization of an X-Band, Non-Coherent Weather Radar", *IEEE*, 1997.

[6] Delrieu, G. et al., "Rain Measurement in Hilly Terrain with X-Band Weather Radar Systems: Accuracy of Path-Integrated Attenuation Estimates Derived from Mountain Returns", *Journal of Atmospheric and Oceanic Technology*, Vol. 16, pp. 405-415, April 1999.

[7] Marzoug, M., Amayenc, P., "Improved Range-Profiling Algorithm of Rainfall Rate from a Spaceborne Radar with Path-Integrated Attenuation Constraint", *IEEE Transactions on Geoscience and Remote Sensing* , Vol. 29, No. 4, pp. 584-592, July 1991.

[8] Meneghini, R. et al., "Estimates of Path Attenuation for the TRMM Radar", *Journal of Atmospheric and Oceanic Technology*, Vol. 16, pp. 405-415, April 1999.

[9] Delrieu, G. et al., "Feasibility of Using Mountain Return for the Correction of Ground-Based X-Band Weather Radar Data", *Journal of Atmospheric and Oceanic Technology*, Vol. 14, pp. 368-385, June, 1997.

[10] M. Bergada, Design and Implementation of a Low Noise Front-End and Internal Calibration Loop for a Ka-Band Cloud Radar., M.S. Thesis, University of Massachusetts at Amherst, May 2001.

[11] Sarabandi, K., Chiu, T., “Optimum Corner Reflectors for Calibration of Imaging Radars”, *IEEE*, 1995.

[12] Probert-Jones, J.R.: “The Radar Equation in Meteorology”, *Quarterly Journal of the Royal Meteorological Society*, Vol. 88, pp 485-495, 1962.

[13] Doviak, R.J., Zrnić, D.S., Doppler Radar and Weather Observations, 2nd ed., Dover Publications, INC.: New York, 1993.

[14] Santiago, J., “Student Led Test Bed GIS Based Vulnerability Assessment of Possible Radar Locations in Western Puerto Rico”, unpublished.

[15] Junyent, F., The Design, Development and Initial Field Deployment of an X-Band Polarimetric Doppler Weather Radar., M.S. Thesis, University of Massachusetts at Amherst, September 2003.

[16] Maeso, J., DSD Characterization and Computations of Expected Reflectivity using Data from a Two-Dimensional Video Disdrometer Deployed in Puerto Rico., M.S. Thesis, University of Puerto Rico at Mayagüez, August 2005.

[17] Mahafza, B.R., Radar Systems: Analysis and Design Using Matlab, 2nd ed., Chapman and Hall/CRC: Boca Raton, FL, 2005.

[18] P. Peebles, Jr., Radar Principles, 1st ed., Wiley Inter-Science: New York, 1998.

[19] Pozar, D.M., Microwave Engineering, 2nd ed., Wiley: New York, 1998.

[20] Arias, D., Rivera W., “Using Grid Computing to Enable Distributed Radar Data Retrieval and Processing”, *IEEE Workshop on Adaptive Grid Computing*, 2006.

[21] Bringi, V.N., and V. Chandrasekar, Polarimetric Doppler Radar, 1st ed., Cambridge University Press: Cambridge, UK, 2001.

[22] G. Heymsfield (private communication), 2007.

[23] The Ohio State University Atmospheric Sciences Program, “Convective Available Potential Energy (CAPE) Help Page”, October 2007, http://twister.sbs.ohio-state.edu/helpdocs/cape.html.

APPENDIX A MATLAB CODE FOR ZH PPI DISPLAY

```
% % % % % % % % % % % % % % % % % % % % % % % % % % % % % % % % % % % % % %
%                                                                         %
%    PR1 PPI Plotter                                                      %
%    Output – Reflectivity PPI Plot  from PR1 Raw Data                    %
%    By: Manuel A. Vega-Cartagena                                         %
%                                                                         %
% % % % % % % % % % % % % % % % % % % % % % % % % % % % % % % % % % % % % %


clc
clear all

c = 3e+8;
kw = 0.885;                              % Refractive index of water (magnitude - X-Band).
f = 9.417;                               % User input.
pt = 25;
g = 38;
pw = 1;
thetah = 2;
thetav = 2;
lr = 0.6066;                             % Receiver loss.
Pnoise = -94.8;
elev = 5.5*(pi/180);

f = f*1e9;
lambda = (c/f)*100;                      % Wavelength in cm.
pt = pt*1000;                            % Transmitted Power in W.
g = 10^(g/10);                           % Linear antenna gain.
lr = 10^(lr/10);                         % Linear receiver loss.

file = input('Enter DAT File Name:  ', 's');
data = load(file);
data_1 = data(:,1);
encoder = data(:,2);

index = 1:361e+3;                        %  Truncating data to gates per profile * 361 (1deg/profile).
data_1 = data_1(index, 1);
encoder = encoder(index, 1);

cal = input('Enter Rx Calibration Coefficients (ax + b) in vector form:  ');

Pr_dBm = (data_1-cal(2))./(cal(1));
Pr = (10.^(Pr_dBm/10));                  % Received Power (mW).
Pnoise = (10^(Pnoise/10));

sr = 5;
gates_number = 1000;
```

```
RangeToFirstGate = input('Range to First Gate (in gates):  ');
sr = sr * 1e+6;
gate = ((c*(1/sr))/2)/1000;                          % in km.
gates = (gate*RangeToFirstGate):gate:(30 - gate);
gates = gates * cos(elev);                           % Adjusting range calculation.
radials = 361;

A = ((pi^5)*(1e-17)*pt*(g^2)*pw*thetah*thetav*(kw));

k = RangeToFirstGate  + 1;
for n = 1:radials;

   for m = 0:((gates_number - RangeToFirstGate)-1);

      Z(n,m+1) = (((6.75*(2^14))*log(2)*(gates(m+1)^2)*(lambda^2)*(Pr(k + m))*lr)/A);
      ZdB(n,m+1) = 10*log10(Z(n,m+1));

   end
   k = k + gates_number;
end

azimuth = 90:-1:-(360 - 90);

THETA = azimuth';
RHO = gates;
for i = 1:length(THETA)
   for j = 1:length(RHO)
      [X(i,j),Y(i,j)] = pol2cart(THETA(i)*pi/180,RHO(j));
   end
end

pcolor(X,Y,ZdB)

   axis equal tight
   shading 'interp'
   caxis ([-10 60])
   colorbar('FontSize',12)
   set(gca,'FontSize',12)
   title('CASA STB PR1 Reflectivity','FontSize',12)
   xlabel('Range (km)','FontSize',12)
   ylabel('Range (km)','FontSize',12)
   h = colorbar;
   hTitle = get(h,'Title');
   set(hTitle,'String','dB_Z')
```

APPENDIX B MATLAB CODE FOR BEAM HEIGHT CALCULATIONS

```
% % % %
```

APPENDIX C MATLAB CODE FOR RADAR EXPECTED SENSITIVITY

```
% % % % % % % % % % % % % % % % % % % % % % % % % % % % % % % % % % % % % %
%                                                                         %
%   Radar Sensitivity - Signal to Noise Ratio                             %
%   as a Function of Range                                                %
%   By: Manuel A. Vega-Cartagena                                          %
%                                                                         %
% % % % % % % % % % % % % % % % % % % % % % % % % % % % % % % % % % % % % %

%  NOTE: This code plots the radar's signal to noise ratio for different
%        rain rates presuming a Rosenfeld Tropical Convetive Z-R
%        relationship. A rain attenuation k-R relationship was presumed as
%        well.

clc
clear all

c = 3e+8;
kw = 0.885;                                     % Refractive index of water (magnitude - X-Band).
f = input('Enter Radar Frequency (GHz):  ');    % User input.
pt = input('Enter Peak Transmitter Power (kW):  ');
Pmin = input('Enter Minimum Detectable Signal Power (dBm):  ');
g = input('Enter Antenna Gain (dB):  ');
thetah = input('Enter Horizontal Antenna BW (deg):  ');
thetav = input('Enter Vertical Antenna BW (deg):  ');
pw = input('Enter Pulse Width (us):  ');

f = f*1e9;
lambda = (c/f)*100;                             % Wavelength in cm.
pt = pt*1000;                                   % Transmitted Power in W.
Pmin = (10^(Pmin/10));                          % Minimum received power mW.
g = 10^(g/10);                                  % Linear antenna gain.

Rr = [1 10 20 30 40];                           % Rain rate vector (mm/hr).
R = 0.15:0.015:30;                              % Distance vector (km).
Pri = zeros(length(Rr),length(R));

for n = 1:length(R)

   for m = 1:length(Rr)

      Kr = 0.01.*Rr(m).^1.21;                   % Rain attenuation (k-R).
      pl = Kr*R(n);                             % Path loss.
      pl = 10^(-pl/10);
      Z = 250.*Rr(m).^1.2;                      % Rosenfeld Tropical Convective Z-R.
      A = ((pi^5)*(1e-17)*pt*(g^2)*pw*thetah*thetav*(kw)*(pl^2)*Z);
      Pri(m,n) = (((6.75*(2^14))*log(2).*(R(n).^2).*(lambda^2))/A);          % Received Power (mW).
```

```
   end
end

Pr = 1./Pri;
SNR = Pr./Pmin;
SNR_dB = 10.*log10(SNR);

figure(1)
plot(R,SNR_dB(1,:),'b','linewidth',1.4)
title('Single Pulse SNR vs Range for Different Rain Rates (Z=250R^1^.^2)')
xlabel('Range (km)')
ylabel('SNR (dB)')
hold on
plot(R,SNR_dB(2,:),'r','linewidth',1.4)
plot(R,SNR_dB(3,:),'g','linewidth',1.4)
plot(R,SNR_dB(4,:),'m','linewidth',1.4)
plot(R,SNR_dB(5,:),'k','linewidth',1.4)
legend('Rain Rate = 1 mm/hr', 'Rain Rate = 10 mm/hr', 'Rain Rate = 20 mm/hr', 'Rain Rate = 30 mm/hr', 'Rain
Rate = 40 mm/hr')
hold off
```

APPENDIX D MATLAB CODE FOR RADAR DIFFERENCE BETWEEN TWO SCANS

```
% % % % % % % % % % % % % % % % % % % % % % % % % % % % % % % % % % % % % %
%                                                                         %
%    PR-1 PPI Plotter - Difference                                        %
%                                                                         %
%    By: Manuel A. Vega-Cartagena                                         %
%                                                                         %
% % % % % % % % % % % % % % % % % % % % % % % % % % % % % % % % % % % % % %


clc
clear all

c = 3e+8;
kw = 0.885;                                 % Refractive index of water (magnitude - X-Band).
f = 9.417;                                  % User input.
pt = 25;
g = 38;
pw = 1;
thetah = 2;
thetav = 2;
lr = 0.6066;                                % Receiver loss.
Pnoise = -94.8;

f = f*1e9;
lambda = (c/f)*100;                         % Wavelength in cm.
pt = pt*1000;                               % Transmitted Power in W.
g = 10^(g/10);                              % Linear antenna gain.
lr = 10^(lr/10);                            % Linear receiver loss.

file = input('Enter DAT File 1 Name:  ', 's');
data = load(file);
data_1 = data(:,1);
encoder = data(:,2);
file_2 = input('Enter DAT File 2 Name:  ', 's');
data2 = load(file_2);
data_2 = data2(:,1);
encoder_1 = data2(:,2);


index = 1:361e+3;                           %  Truncating data to gates per profile * 361 (1deg/profile).
data_1 = data_1(index, 1);
encoder = encoder(index, 1);
data_2 = data_2(index,1);
encoder_1 = data_2(index,1);

cal = input('Enter Rx Calibration Coefficients (ax + b) in vector form:  ');
```

```
Pr_dBm = (data_1-cal(2))./(cal(1));
Pr = (10.^(Pr_dBm/10));                          % Received Power (mW).
Pnoise = (10^(Pnoise/10));
Pr_dBm_2 = (data_2-cal(2))./(cal(1));
Pr_2 = (10.^(Pr_dBm_2/10));                       % Received Power (mW).

sr = 5;
gates_number = 1000;
RangeToFirstGate = input('Range to First Gate (in gates):  ');
sr = sr * 1e+6;
gate = ((c*(1/sr))/2)/1000;                       % in km.
gates = (gate*RangeToFirstGate):gate:(30 - gate);
radials = 361;

A = ((pi^5)*(1e-17)*pt*(g^2)*pw*thetah*thetav*(kw));

k = RangeToFirstGate  + 1;
for n = 1:radials;

   for m = 0:((gates_number - RangeToFirstGate)-1);

      Z(n,m+1) = (((6.75*(2^14))*log(2)*(gates(m+1)^2)*(lambda^2)*(Pr(k + m))*lr)/A);
      ZdB(n,m+1) = 10*log10(Z(n,m+1));

   end
   k = k + gates_number;
end

k = RangeToFirstGate  + 1;
for n = 1:radials;

   for m = 0:((gates_number - RangeToFirstGate)-1);

      Z_2(n,m+1) = (((6.75*(2^14))*log(2)*(gates(m+1)^2)*(lambda^2)*(Pr_2(k + m))*lr)/A);
      ZdB_2(n,m+1) = 10*log10(Z_2(n,m+1));

   end
   k = k + gates_number;
end

ZdB_Diff = ZdB_2 - ZdB;

azimuth = 90:-1:-(360 - 90);

THETA = azimuth';
RHO = gates;
for i = 1:length(THETA)
   for j = 1:length(RHO)
      [X(i,j),Y(i,j)] = pol2cart(THETA(i)*pi/180,RHO(j));
   end
end
```

```
pcolor(X,Y,ZdB_Diff)

    axis equal tight
    shading 'interp'
    caxis ([-10 70])
    colorbar('FontSize',12)
    set(gca,'FontSize',12)
    title('CASA STB PR1 Reflectivity','FontSize',12)
    xlabel('Range (km)','FontSize',12)
    ylabel('Range (km)','FontSize',12)
    h = colorbar;
    hTitle = get(h,'Title');
    set(hTitle,'String','dB_Z')
```